



ARTICLE

Midkine drives cardiac inflammation by promoting neutrophil trafficking and NETosis in myocarditis

Ludwig T. Weckbach^{1,2,3,4*}, Ulrich Grabmaier^{1,4*}, Andreas Uhl^{1,2,3}, Sebastian Gess^{2,3}, Felicitas Boehm^{2,3}, Annette Zehrer^{2,3}, Robert Pick^{2,3}, Melanie Salvermoser^{2,3}, Thomas Czermak¹, Joachim Pircher¹, Noah Sorrelle⁵, Mary Migliorini⁶, Dudley K. Strickland⁶, Karin Klingel⁷, Volker Brinkmann^{8,9}, Ulrike Abu Abed^{8,9}, Urs Eriksson^{10,11} , Steffen Massberg^{1,4}, Stefan Brunner^{1*}, and Barbara Walzog^{2,3*} 

Heart failure due to dilated cardiomyopathy is frequently caused by myocarditis. However, the pathogenesis of myocarditis remains incompletely understood. Here, we report the presence of neutrophil extracellular traps (NETs) in cardiac tissue of patients and mice with myocarditis. Inhibition of NET formation in experimental autoimmune myocarditis (EAM) of mice substantially reduces inflammation in the acute phase of the disease. Targeting the cytokine midkine (MK), which mediates NET formation in vitro, not only attenuates NET formation in vivo and the infiltration of polymorphonuclear neutrophils (PMNs) but also reduces fibrosis and preserves systolic function during EAM. Low-density lipoprotein receptor-related protein 1 (LRP1) acts as the functionally relevant receptor for MK-induced PMN recruitment as well as NET formation. In summary, NETosis substantially contributes to the pathogenesis of myocarditis and drives cardiac inflammation, probably via MK, which promotes PMN trafficking and NETosis. Thus, MK as well as NETs may represent novel therapeutic targets for the treatment of cardiac inflammation.

Introduction

Myocarditis is the underlying cause of dilated cardiomyopathy (DCM) in 20–50% of DCM patients in Europe and North America (Cooper et al., 2014). While acute myocarditis is often triggered by cardiotropic viruses (e.g., enteroviruses, adenoviruses, parvovirus B19 [PVB19], and others), transition to autoimmune-mediated inflammation may sustain myocarditis upon eradication of the virus, eventually leading to an end-stage heart failure phenotype of inflammatory DCM (Caforio et al., 2013). The involvement of adaptive immunity in the pathogenesis of myocarditis and inflammatory DCM has been widely acknowledged and investigated (Heymans et al., 2016). However, the role of the innate immune response, especially polymorphonuclear neutrophils (PMNs) as potential drivers of persistent cardiac inflammation, has only been marginally addressed. PMNs can maintain inflammation by a specific process called NETosis (Warnatsch et al., 2015). Upon activation by various stimuli,

including viruses, bacteria, or cytokines, PMNs eject their DNA decorated with antimicrobial proteins (e.g., myeloperoxidase [MPO] or neutrophil elastase [NE]; Brinkmann et al., 2004; Kenny et al., 2017; Toussaint et al., 2017). Neutrophil extracellular traps (NETs) can enhance inflammation as well as tissue injury by different mechanisms, including direct damage, platelet activation, triggering autoantibody production, and reducing the threshold for T cell activation (Tillack et al., 2012; Sørensen and Borregaard, 2016; Martinod et al., 2017; McDonald et al., 2017; Nakazawa et al., 2017).

PMNs are recruited to the tissue during inflammation, where they can undergo NETosis. The 13-kD cytokine midkine (MK) is critical for PMN adhesion and subsequent extravasation during acute inflammation (Weckbach et al., 2014) and mediates immune cell recruitment in chronic inflammation in mouse models of multiple sclerosis or rheumatoid arthritis (Maruyama

¹Medizinische Klinik und Poliklinik I, Klinikum der Universität, Ludwig-Maximilians-University Munich, Munich, Germany; ²Walter Brendel Centre of Experimental Medicine, University Hospital, Ludwig-Maximilians-University Munich, Planegg-Martinsried, Germany; ³Institute of Cardiovascular Physiology and Pathophysiology, Biomedical Center, Ludwig-Maximilians-University Munich, Planegg-Martinsried, Germany; ⁴German Center for Cardiovascular Research, Partner Site Munich Heart Alliance, Munich, Germany; ⁵Hamon Center for Therapeutic Oncology Research, Division of Surgical Oncology, Department of Surgery, University of Texas Southwestern Medical Center, Dallas, TX; ⁶Center for Vascular and Inflammatory Disease, Departments of Surgery and Physiology, University of Maryland School of Medicine, Baltimore, MD; ⁷Cardiopathology, Institute for Pathology and Neuropathology, University Hospital Tuebingen, Tuebingen, Germany; ⁸Microscopy Core Facility, Max Planck Institute for Infection Biology, Berlin, Germany; ⁹Department of Cellular Microbiology, Max Planck Institute for Infection Biology, Berlin, Germany; ¹⁰Cardioimmunology, Center for Molecular Cardiology, University of Zurich, Zurich, Switzerland; ¹¹Department of Medicine, Gesundheitsversorgung Zürcher Oberland-Zürich Regional Health Center, Wetzikon, Switzerland.

*L.T. Weckbach, U. Grabmaier, S. Brunner, and B. Walzog contributed equally to this paper; Correspondence to Barbara Walzog: walzog@lrz.uni-muenchen.de; Ludwig T. Weckbach: ludwig.weckbach@med.lmu.de.

© 2019 Weckbach et al. This article is distributed under the terms of an Attribution–Noncommercial–Share Alike–No Mirror Sites license for the first six months after the publication date (see <http://www.rupress.org/terms/>). After six months it is available under a Creative Commons License (Attribution–Noncommercial–Share Alike 4.0 International license, as described at <https://creativecommons.org/licenses/by-nc-sa/4.0/>).

et al., 2004; Wang et al., 2008). Restrictive expression under physiological conditions in adults makes MK an interesting therapeutic target (Muramatsu and Kadomatsu, 2014). Previous data suggested that MK mediates PMN adhesion by binding to the low-density lipoprotein receptor-related protein 1 (LRP1), a member of the low-density lipoprotein (LDL) receptor family (Weckbach et al., 2014). LRP1 is a widely expressed transmembrane receptor that is primarily involved in endocytosis of extracellular proteins or other cell surface receptors (Lillis et al., 2008). In addition, LRP1 can interact with transmembrane receptors, modulating intracellular signaling upon ligand binding. In macrophages, LRP1 interacts with adhesion molecules of the β_2 integrin family, which are critical for PMN recruitment and activation during inflammation (Ranganathan et al., 2011; Herter and Mayadas, 2014). However, the potential impact of the MK-LRP1 axis on PMN recruitment during acute or chronic inflammation is still unknown.

In this study, we identify NETs in endomyocardial biopsies (EMBs) of patients suffering from myocarditis. Moreover, we decipher the functional importance of NETs for myocarditis and delineate the mechanistic link between NETs and MK. We report a new molecular axis between MK and LRP1 that is critical for β_2 integrin-dependent PMN recruitment steps and the formation of NETs. In a mouse model of myocarditis, targeting NETs or MK inhibits the development of the disease and preserves heart function.

Results

Targeting MK reduces PMN infiltration and NETosis in the inflamed myocardium

Initially, we explored the presence of NETs in myocardial tissue of patients with acute myocarditis. Clinical patient characteristics are shown in Table 1. In paraffin-embedded sections of EMBs from 14 individuals with myocarditis, we were able to detect NETs in EMBs of two patients with evidence of PVB19 infection and in all eight patients without evidence of PVB19 infection (Table 1). NETs were identified by the colocalization of the H2A–H2B–DNA complex, MPO, and citrullinated histone 3 (H3Cit). PMN infiltration was found in EMBs of all patients. A representative image indicating the presence of NETs in the inflamed cardiac tissue is shown in Fig. 1 a. To study the functional relevance of NETs in myocarditis, we applied a mouse model of experimental autoimmune myocarditis (EAM) using s.c. injection of α myosin heavy chain peptide with CFA and sham-treated animals for control, which received vehicle and CFA. We stained heart sections of mice at day 21 after induction of EAM, which represents the peak of inflammatory infiltrates in this model (Afanasyeva et al., 2001). Here, we were able to detect DNA decorated with NE and H3Cit, indicating the presence of NETs in this model (Fig. 1 d). To elucidate the relevance of NET formation on inflammation, we evaluated leukocyte infiltration in EAM (referred to as EAM score) after treatment of mice with DNase or the protein-arginine deiminase inhibitor Cl-amidine (Cl-amid). Here, DNase was administered twice daily and Cl-amid once daily from day 1 until day 21 after induction of EAM, as illustrated in Fig. S1 a. Leukocyte infiltration in EAM mice was significantly increased

compared with sham-treated control mice (sham, Fig. 1 b). Strikingly, treatment with DNase or Cl-amid significantly reduced leukocyte infiltration to levels of sham-treated control mice. Moreover, the heart/body weight ratio of EAM mice treated with DNase or Cl-amid was significantly diminished compared with vehicle-treated EAM mice (Fig. 1 c). As expected, NET formation (indicated by H3Cit and NE staining in the cardiac tissue) was reduced compared with vehicle-treated mice after targeting NETs (Fig. S1 b). In cardiac sections of sham-treated control mice without induction of EAM, no NETs were detectable. These findings suggest that NETs promote cardiac inflammation during EAM. Since the cytokine MK is critical for PMN adhesion and subsequent recruitment during inflammatory processes (Weckbach et al., 2014), we investigated whether MK impacts PMN infiltration in our model. First, we evaluated whether MK expression is altered during cardiac inflammation. Indeed, MK mRNA expression was significantly increased in cardiac tissue of EAM mice at day 21 compared with sham-immunized mice at the same time point (Fig. S2 a). Next, MK was targeted with an antibody (Ab) specifically blocking the N-terminal domain of MK (anti-N-MK). Here, the anti-N-MK Ab was administered twice a week from day 1 until day 21 after induction of EAM, as illustrated in Fig. S2 b. Using this approach, we found a substantially reduced number of infiltrated PMN in EAM mice (768 ± 55 vs. 158 ± 86 PMN/mm²; Fig. 1, e and f). In line with this observation, the absolute number of NET⁺ PMNs was significantly reduced after blocking MK during EAM compared with vehicle-treated EAM mice (40 ± 6 vs. 5 ± 2 NET⁺ PMN; Fig. 1 g). Strikingly, the number of NET⁺ PMNs in the percentage of all extravasated PMNs was also dramatically decreased after inhibition of MK compared with vehicle-treated EAM mice (5.1 ± 0.5 vs. 0.9 ± 0.6 NET⁺ PMN [%]; Fig. 1 h), suggesting a contribution of MK on NETosis on top of its effects on PMN recruitment.

The N-terminal domain of MK is critical for PMN infiltration in myocarditis

Next, we elucidated the impact of MK on the acute phase of myocarditis. Histological analysis of leukocyte infiltration in myocardial sections revealed a significantly diminished number of infiltrated leukocytes after application of the anti-N-MK Ab compared with vehicle-treated mice at day 21 after induction of EAM (Fig. 2 a). Similar to the findings after treatment with DNase or Cl-amid, the heart/body weight ratio was significantly reduced upon administration of the anti-N-MK Ab, suggesting that blocking MK protects the heart from the deteriorating effect of myocarditis (Fig. 2 b). To study whether infiltration of specific leukocyte subsets in EAM was affected by MK blockade, we investigated digested hearts of EAM mice upon administration of the anti-N-MK Ab or isotype control treatment at day 21 after induction of EAM using flow cytometry. By staining the pan-leukocyte marker CD45, we were able to confirm that infiltration of leukocytes was significantly diminished after MK inhibition compared with the isotype control (Fig. 2 c). Administration of the anti-N-MK Ab significantly reduced the number of CD45⁺/CD11b⁺/Gr-1⁺ cells compared with isotype controls. Similar results were obtained by analysis of Ly6G⁺ cells. This effect was not observed in the CD45⁺/CD11b⁺/Gr-1[−] cell population predom-

Table 1. Patients with myocarditis

Patient	Age	Sex	IHC ^a	PVB19	PMN	NETs	Medication	Symptoms	LVEF at diagnosis (%)	Follow up (yr)	LVEF at follow up
1	47	f	+	+	+	–	BB, ACEI, diuretics	Heart failure	10	3	32%
2	29	f	+	+	+	–	BB, ACEI, MRA, diuretics	Heart failure	28	11	41%
3	48	m	+	+	+	–	BB, ACEI, MRA, diuretics	Heart failure	29	None	—
4	36	m	+	+	+	–	BB, ACEI, corticosteroids	Cardiac arrest	30	<1	Normalized
5	44	m	+	+	+	+	BB, ACEI, diuretics	Heart failure and angina pectoris	37	None	—
6	30	f	+	+	+	+	BB, ACEI, diuretics	Heart failure	45	10	Normalized
7	24	f	+	–	+	+	ACEI	LV thrombus	Normal	None	—
8	55	m	+	–	+	+	BB, ACEI	Heart failure	30	10	Normalized
9	75	f	+	–	+	+	BB, MRA, diuretics	Angina pectoris	30	None	—
10	46	m	+	–	+	+	BB, ACEI, MRA, diuretics	Heart failure	27	<1	40%
11	64	m	+	–	+	+	BB, ACEI, diuretics	Heart failure	25	<1	27%
12	56	m	+	–	+	+	BB, ACEI, MRA, diuretics	Heart failure	18	<1	45%
13	Unknown	m	+	–	+	+	Unknown	Unknown	Unknown	Unknown	Unknown
14	37	m	+	–	+	+	BB, ACEI, MRA, diuretics	Heart failure	23	None	—

ACEI, angiotensin-converting enzyme inhibitor; BB, beta blocker; f, female; LV, left ventricle; LVEF, left ventricular ejection fraction; m, male; MRA, mineralocorticoid receptor antagonist.

^a≥ 14 leukocytes/mm² and HLA-DR overexpression.

inantly consisting of monocytes and macrophages. However, targeting the N-terminal domain of MK led to a reduced infiltration of CD4⁺ T helper cells, whereas proliferation of splenic CD4⁺ T cells after stimulation with anti-CD3/CD28 beads was not affected by blocking MK, indicating that targeting the N-terminal domain of MK did not attenuate T cell proliferation (Fig. S2 c). Moreover, expression of the classical proinflammatory cytokine macrophage inflammatory protein 2- α (MIP2- α) was not significantly changed after blocking MK, suggesting that MK may not simply exert its effect by promoting expression of proinflammatory cytokines (Fig. S2 d). Interestingly, blocking the C-terminal MK domain (anti-C-MK) did not reduce infiltration of CD45⁺, CD45⁺/CD11b⁺/Gr-1⁺, CD45⁺/CD11b⁺/Gr-1⁺ or CD4⁺ cells compared with the appropriate isotype control in our model (Fig. 2 d), suggesting that the N-terminal domain of MK, but not the C-terminal domain, is critically required for leukocyte infiltration in this model. Interestingly, MK was expressed in the perivascular compartment of the inflamed cardiac tissue, suggesting that it may directly foster leukocyte infiltration in this model, as described earlier for the inflamed mouse cremaster muscle model (Weckbach et al., 2014; Fig. 2 e). Blood vessel-associated MK expression was not detectable in the cardiac tissue obtained from sham-treated control mice.

Targeting MK reduces postinflammatory fibrosis and heart failure

To determine whether MK-mediated leukocyte infiltration affects transition to postinflammatory fibrosis and dysfunction of the heart, we evaluated cardiac fibrosis and dysfunction after

anti-N-MK Ab or vehicle treatment at day 63 of EAM. We evaluated the amount of collagen in cardiac muscle sections as an indicator for cardiac fibrosis after Masson's trichrome staining (Fig. 3 a). As expected, detailed analysis using a semiquantitative fibrosis score revealed a significant increase of fibrotic tissue in the myocardium of EAM mice compared with sham-treated control animals (Fig. 3 b). MK blockade with an anti-N-MK Ab significantly reduced fibrosis compared with vehicle-treated EAM mice. No effect was observed for IgG1 isotype Ab-treated mice compared with vehicle-treated animals (Fig. S3 a). These findings suggest that inhibition of MK not only diminishes leukocyte infiltration into the cardiac tissue but also reduces cardiac fibrosis. Next, we studied whether blocking MK also protects systolic function during EAM. Transthoracic echocardiography at day 63 (Fig. 3 c) revealed that fractional shortening (Fig. 3 d) as well as left ventricular ejection fraction (Fig. 3 e) were significantly preserved in anti-N-MK Ab-treated, but not vehicle-treated, EAM mice compared with sham-treated control animals (Fig. 3, d and e; and Video 1). There was no difference between treatment with vehicle or anti-N-MK Ab-matched IgG1 isotype control (Fig. S3, b and c). These results implicate that MK plays a role for inflammation and cardiac dysfunction in this model. To study whether anti-N-MK Ab was able to inhibit leukocyte adhesion, the critical prerequisite for extravasation, we conducted intravital microscopy of postcapillary venules in the cremaster muscle 2 h after intrascrotal application of TNF α , which mainly attracts PMNs within this time period (Weckbach et al., 2014; see also Fig. 4 e). Consistent with the results in MK^{-/-} animals in this model (Weckbach et al., 2014), rolling flux fraction and

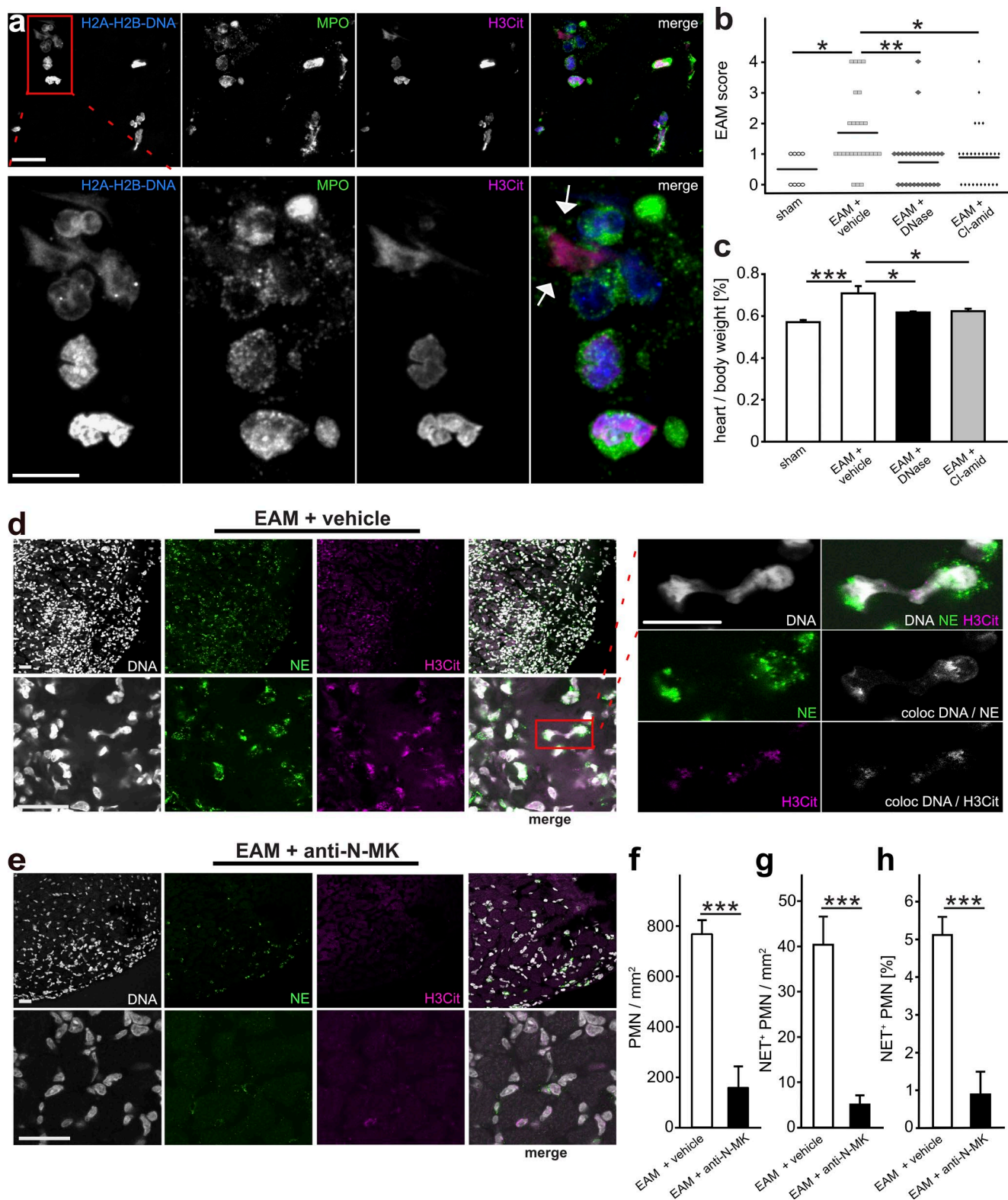


Figure 1. NETs contribute to the pathogenesis of myocarditis. (a) Confocal immunofluorescence images of an EMB of patient 6 suffering from PVB19-positive myocarditis (see Table 1). Top: Images show staining of H2A-H2B-DNA, MPO, and H3Cit as well as the merged image. Bar, 20 μ m. Bottom: Magnification of a selected area of the merged confocal image (box) from the top panel. Arrows indicate NETs. Bar, 10 μ m. **(b and c)** EAM score (b) as well as evaluation of the heart/body weight ratio (c) at day 21 after induction of EAM or sham immunization (sham; mean EAM score, 0.5 ± 0.19 ; mean heart/body weight ratio, 0.57 ± 0.01). Mice were treated with DNase (EAM + DNase: mean EAM score, 0.8 ± 0.19 ; mean heart/body weight ratio, 0.62 ± 0.005), Cl-amid (EAM + Cl-amid: mean EAM score, 0.9 ± 0.20 ; mean heart/body weight ratio, 0.62 ± 0.01), or vehicle as control (EAM + vehicle: mean EAM score, 1.7 ± 0.25 ; mean heart/body weight ratio, 0.71 ± 0.04) as indicated. $n = 8$ for sham group; $n = 26$ for EAM groups. **(d)** Left: Representative confocal images of cardiac sections of immunized WT mice at day 21 after induction of EAM (EAM + vehicle). Images show staining of DNA, NE, and H3Cit as well as the merged image. Bars, 20 μ m. Right:

rolling velocity were not affected by blocking MK (Fig. 3, f and g). However, adhesion was significantly reduced after treatment with the anti-N-MK Ab compared with the appropriate isotype control (Fig. 3 h). Hematopoietic parameters were not affected by the anti-N-MK Ab (Fig. 3 i). Thus, the anti-N-MK Ab was able to significantly inhibit leukocyte trafficking in inflammation.

The MK receptor LRP1 is critical for PMN recruitment and cardiac inflammation

Previous data suggested that LRP1 may represent the functional receptor for MK on PMN during the recruitment process (Weckbach et al., 2014). To investigate whether PMN trafficking is compromised in the absence of LRP1, we performed intravital microscopy in postcapillary venules of the cremaster muscle 2 h after intrascrotal application of TNF α in *LRP1^{fl/fl}/vav-cre⁻* (*LRP1^{ctrl}*) and *LRP1^{fl/fl}/vav-cre⁺* (*LRP1^{CKO}*) mice with a specific knock-out of LRP1 in the hematopoietic system (Fig. S4, a and b). Rolling flux fraction as well as rolling velocity were not altered in the absence of LRP1 compared with control mice (Fig. 4, a and b). However, leukocyte adhesion was significantly reduced in *LRP1^{CKO}* animals compared with *LRP1^{ctrl}* mice to a similar extent as after blocking MK (Fig. 4 c and Video 2). Hematopoietic parameters were similar in both mouse strains (Fig. 4 d). Extravasation of PMN into the inflamed cremaster muscle tissue was significantly compromised in the absence of LRP1 in the hematopoietic system when compared with control animals in this model, as analyzed by histology (Fig. S4 c and Fig. 4 e). In contrast, diminished recruitment of eosinophils or lymphocytes, basophils, and monocytes ("Others") was not detected in *LRP1^{CKO}* compared with *LRP1^{ctrl}* mice in this model (Fig. 4 e). To investigate whether LRP1 may also be important during EAM, we targeted LRP1 using the inhibitor receptor-associated protein (RAP), which blocks all members of the LDL receptor family. Here we used a chemically modified more stable form of RAP (Prasad et al., 2015). Due to fast clearance of RAP, miniosmotic pumps releasing RAP constantly were s.c. implanted. Continuous RAP administration over 21 d after induction of EAM reduced leukocyte infiltration in EAM mice significantly compared with vehicle-treated control mice (Fig. S4, d and e), suggesting that LRP1 may be functionally involved in cardiac inflammation. To study whether LRP1 may regulate the function of the β_2 integrin lymphocyte function-associated antigen 1 (LFA-1; CD11a/CD18), which is critical for induction of PMN adhesion in the cremaster model (Ding et al., 1999), we analyzed the colocalization of LRP1 and CD11a using spinning-disk confocal microscopy of murine WT PMN (mPMN) in microflow chambers in vitro. We found increased colocalization and clustering of LRP1 with CD11a on the cell surface exclusively upon adhesion

(Fig. 4, f and g; and Video 3). Quantitative analysis revealed a significantly elevated intensity per colocalization area of LRP1 and CD11a after adhesion compared with rolling, confirming the rising colocalization of both molecules upon the onset of adhesion (Fig. 4 h). To rule out unspecific clustering and colocalization, we analyzed the cell surface expression of LRP1 and Gr-1 as control during the process of rolling and adhesion (Fig. 4 f). We found clustering of LRP1 during adhesion but no specific colocalization between LRP1 and Gr-1 in the clustered cell surface area (Fig. 4 g and Video 4). Accordingly, the intensity of the area of colocalization of LRP1 and Gr-1 did not increase during transition from rolling to adhesion (Fig. 4 h). These findings indicate that LRP1 and CD11a specifically cluster and colocalize upon induction of adhesion during PMN recruitment. However, the genetic absence of LRP1 on PMN did not affect the affinity regulation of LFA-1 as measured by flow cytometry using LFA-1-specific intercellular adhesion molecule 1 (ICAM-1) binding (data not shown). We could exclude altered cell surface expression of β_2 integrins in the absence of LRP1 as a cause of reduced PMN adhesion (Fig. S5 a).

MK specifically induces LRP1-mediated PMN trafficking

To investigate the functional impact of LRP1 on PMN trafficking, we generated Hoxb8 stem cell factor (SCF) cells (referred to as Hoxb8 cells) from the bone marrow (BM) of *LRP1^{ctrl}* (*Hoxb8-LRP1^{ctrl}*) and *LRP1^{CKO}* (*Hoxb8-LRP1^{CKO}*) mice (Fig. S5 b). Hoxb8 cells were generated by immortalization of BM progenitor cells using transduction with estrogen-responsive Hoxb8, preventing the differentiation of progenitor cells. Upon removal of estrogen Hoxb8, cells can be differentiated toward PMNs in the presence of SCF (Wang et al., 2006; Redecke et al., 2013). These differentiated (d)Hoxb8 cells behave very similar compared with BM-derived mPMNs and represent a useful tool to study PMN trafficking (Zehrer et al., 2018). Similar to freshly isolated PMNs, we found clustering and colocalization of LRP1 and CD11a on adherent and migrating dHoxb8-*LRP1^{ctrl}* in the presence of immobilized MK (iMK) under flow conditions using stimulated emission depletion (STED) nanoscopy (Fig. 5 a and Video 5). To study the functional impact of the MK-LRP1 axis, we analyzed adhesion of dHoxb8-*LRP1^{ctrl}* and dHoxb8-*LRP1^{CKO}* in microflow chambers in the presence of P-selectin, ICAM-1, and CXCL1 and found no difference between dHoxb8-*LRP1^{ctrl}* and dHoxb8-*LRP1^{CKO}* cells (Fig. 5 b). In sharp contrast, adhesion of dHoxb8-*LRP1^{CKO}* cells was significantly diminished in the presence of immobilized P-selectin, ICAM-1, and MK compared with dHoxb8-*LRP1^{ctrl}* cells, indicating a role of the MK-LRP1 axis for PMN adhesion. Similarly, adhesion strengthening as well as spreading were specifically compromised in

Representative confocal magnified image of NETs. Images show staining of DNA, NE, and H3Cit as well as the merged image, colocalization (coloc) of DNA/NE, and DNA/H3Cit as indicated. Bars, 10 μ m. (e) Representative confocal images of cardiac sections of EAM mice at day 21 after induction of EAM and blockade of MK for 21 d. Images show staining of DNA, NE, and H3Cit as well as the merged image. Bars, 20 μ m. (f–h) Histological analysis of extravasated PMN into the cardiac tissue at day 21 after induction of EAM without blocking MK (EAM + vehicle) or after application of an anti-N-MK blocking Ab (EAM + anti-N-MK). Diagrams show the number of extravasated PMNs per mm² (f: vehicle, 768 \pm 55 PMN/mm²; anti-N-MK, 158 \pm 86 PMN/mm²), the number of NET⁺ PMNs per mm² (g: vehicle, 40 \pm 6 NET⁺ PMN; anti-N-MK = 5 \pm 2 NET⁺ PMN), and the number of NET⁺ PMNs as a percentage of all extravasated PMNs (h: vehicle, 5.1 \pm 0.5 NET⁺ PMN [%]; anti-N-MK, 0.9 \pm 0.6 NET⁺ PMN [%]). *n* = 6 mice. To determine P values, ANOVA on ranks with Dunn's multiple comparisons test was performed for c and d, and an unpaired Student's *t* test was used for f–h. For all panels, *, *P* < 0.05; **, *P* < 0.01; ***, *P* < 0.001. Data are presented as mean \pm SEM or mean \pm individual data points.

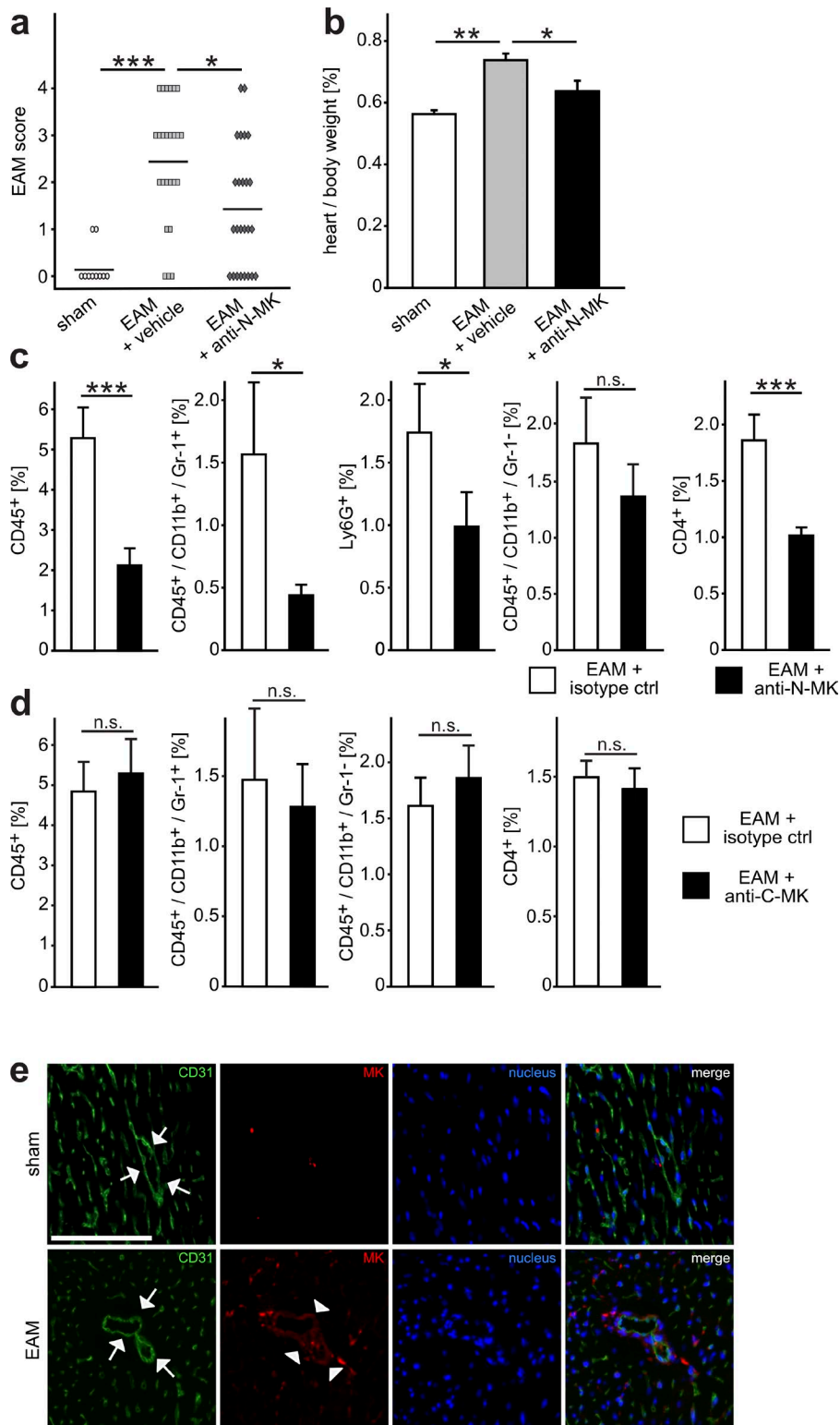


Figure 2. Targeting MK attenuates leukocyte infiltration into the heart during EAM.

(a and b) Semiquantitative histological analysis of leukocyte infiltration (a) and evaluation of the heart/body weight ratio (b) at day 21 after sham immunization (sham: a, mean EAM score, 0.2 ± 0.1; b, mean heart/body weight ratio, 0.56 ± 0.01) or induction of EAM. EAM mice were treated with an anti-N-MK blocking Ab (EAM + anti-N-MK: a, mean EAM score, 1.4 ± 0.27; b, mean heart/body weight ratio, 0.64 ± 0.03) or vehicle alone (EAM + vehicle: a, mean EAM score, 2.5 ± 0.26; b, mean heart/body weight ratio, 0.74 ± 0.02) as depicted. *n* = 10 for sham group; *n* = 25 for EAM groups. (c and d) Flow cytometric analysis of leukocyte subpopulations in the cardiac tissue on day 21 after induction of EAM. Diagrams show the percentage of leukocyte subpopulations of all cells after blocking the N-terminal domain (EAM + anti-N-MK, c; CD45⁺: isotype ctrl, 5.28 ± 0.76 cells [%], anti-N-MK, 2.12 ± 0.42 cells [%]; CD45⁺/CD11b⁺/Gr-1⁺: isotype ctrl, 1.59 ± 0.58 cells [%], anti-N-MK, 0.45 ± 0.08 cells [%]; Ly6G⁺: isotype ctrl, 1.74 ± 0.39 cells [%], anti-N-MK, 0.99 ± 0.28 cells [%]; CD45⁺/CD11b⁺/Gr-1⁻: isotype ctrl, 1.84 ± 0.41 cells [%], anti-N-MK, 1.37 ± 0.29 cells [%]; CD4⁺: isotype ctrl, 1.86 ± 0.23 cells [%], anti-N-MK, 1.02 ± 0.07 cells [%]) or the C-terminal domain of MK (EAM + anti-C-MK, d; CD45⁺: isotype ctrl, 4.86 ± 0.72 cells [%], anti-C-MK, 5.29 ± 0.86 cells [%]; CD45⁺/CD11b⁺/Gr-1⁻: isotype ctrl, 1.61 ± 0.25 cells [%], anti-C-MK, 1.86 ± 0.30 cells [%]; CD4⁺: isotype ctrl, 1.50 ± 0.12 cells [%], anti-C-MK, 1.41 ± 0.15 cells [%]) compared with the matching isotype controls (EAM + isotype ctrl). *n* = 18. (e) Representative immunofluorescence images of cardiac sections of sham-treated mice for control (top) or EAM mice at day 21 after induction of EAM (bottom). Images show staining of CD31, MK, and DAPI as well as the merged image. Arrows indicate a blood vessel. Arrowheads show MK expression in the perivascular compartment. Bars, 100 μm. To determine P values, ANOVA on ranks with Dunn's multiple comparisons test was performed for a and b, and a Mann-Whitney rank sum test was used for c and d. For all panels, *, *P* < 0.05; **, *P* < 0.01; ***, *P* < 0.001; n.s., not significant. Data are presented as mean ± SEM or mean ± individual data points.

dHoxb8-*LRP1*^{KO} compared with dHoxb8-*LRP1*^{ctrl} cells in the presence of MK in contrast to CXCL1 (Fig. S5, c and d). Studying migration using dHoxb8 cells under flow conditions in vitro, the Euclidian distance and migration velocity on immobilized CXCL1 was not altered in the absence of LRP1. However, on iMK, the Euclidian distance and migration velocity were diminished in dHoxb8-*LRP1*^{KO} compared with control cells (Fig. 5, c and d;

Fig. S5 e; and Video 6). Furthermore, in dHoxb8 cells generated from the BM of *LRP1* NPxYxxL knock-in mice (dHoxb8-*LRP1*-NPxY^{KI}) with a nonfunctional membrane distal intracellular NPxY domain, adhesion was significantly reduced compared with control cells (dHoxb8-*LRP1*-NPxY^{ctrl}), suggesting that the membrane distal NPxY domain of LRP1 is involved in MK-mediated adhesion (Fig. 5 e).

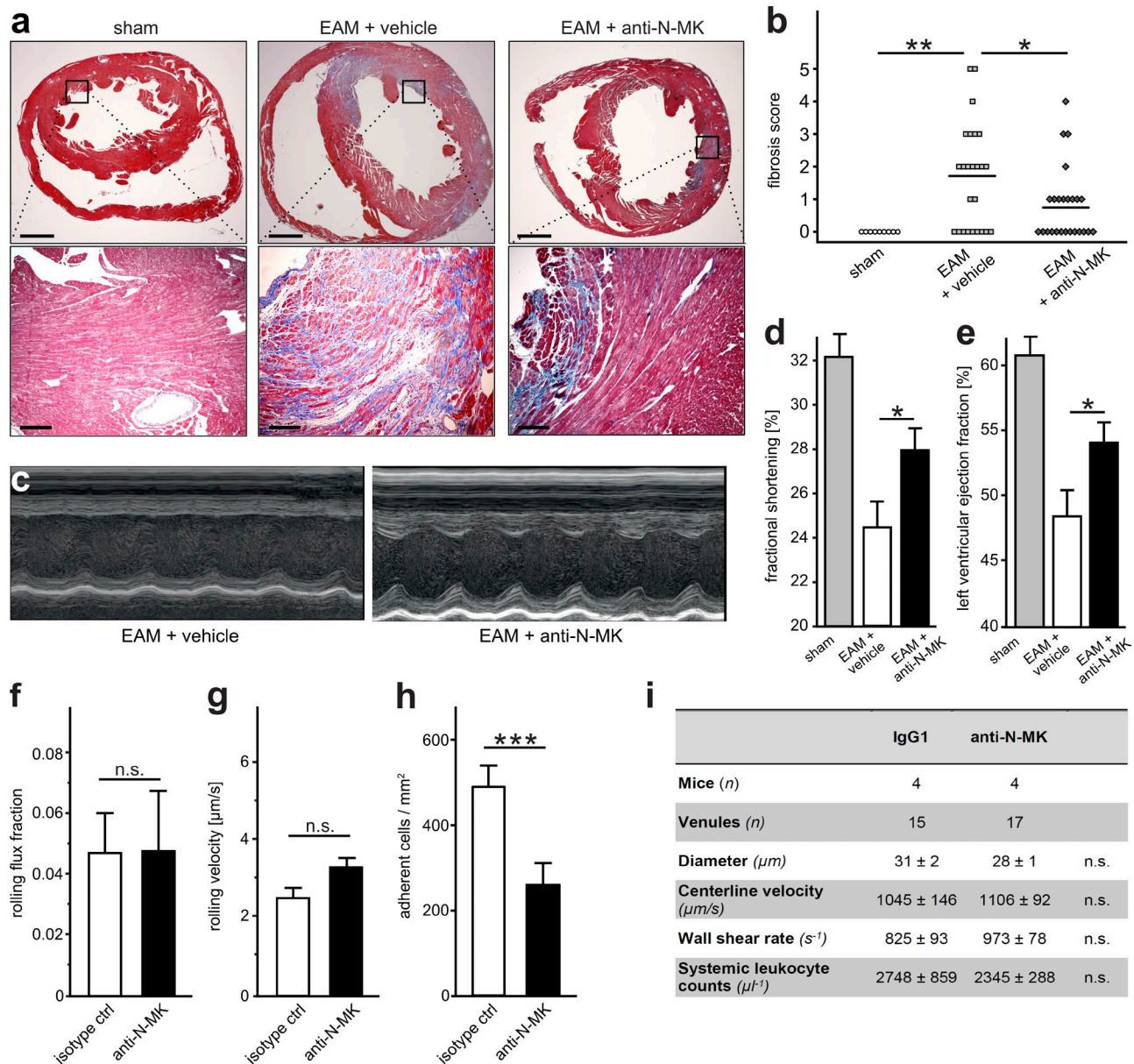


Figure 3. Blocking MK reduces cardiac fibrosis and preserves cardiac function during the chronic phase of myocarditis. (a) Representative cross sections of cardiac tissue of sham-treated control mice, vehicle-treated EAM mice, and EAM mice after anti-N-MK Ab treatment on day 63 using Masson's trichrome staining. Fibrotic tissue appears blue. Bars, 1 mm (overview); 100 μm (magnification). (b) Degree of fibrosis in the cardiac tissue using a semiquantitative score. Single data points represent individual mice (sham: mean fibrosis score, 0 ± 0 ; EAM + vehicle: mean fibrosis score, 1.68 ± 0.32 ; EAM + anti-N-MK: mean fibrosis score, 0.80 ± 0.22). $n = 10$ for sham mice; $n = 25$ for EAM groups. (c) Echocardiographic images on day 63 after immunization. Representative M-mode short axis view images depicting diastolic and systolic diameters of vehicle-treated animals (EAM + vehicle) as well as anti-N-MK Ab-treated mice (EAM + anti-N-MK). (d and e) Parameters describing systolic function using (d) fractional shortening (sham, 32.1 ± 1.0 [%]; EAM + vehicle, 24.4 ± 1.1 [%]; EAM + anti-N-MK, 27.9 ± 1.0 [%]) and (e) left ventricular ejection fraction (sham, 60.8 ± 1.4 [%]; EAM + vehicle, 48.6 ± 1.9 [%]; EAM + anti-N-MK, 54.2 ± 1.5 [%]). $n = 10$ for sham mice; $n = 25$ for the EAM groups. (f–i) Intravital microscopy of cremaster muscle postcapillary venules of WT mice treated with anti-N-MK blocking Ab (anti-N-MK) or the appropriate isotype Ab (isotype ctrl) as control 2 h after intrascrotal application of TNF α . $n = 15$ venules from four mice (isotype ctrl); $n = 17$ venules from four mice (anti-N-MK). (f) Leukocyte rolling flux fraction (isotype control, 0.047 ± 0.013 [%]; anti-N-MK, 0.048 ± 0.019 [%]). (g) Leukocyte rolling velocity including 35 cells from four control mice (isotype ctrl) and 41 cells from four mice after blocking MK (anti-N-MK; isotype ctrl, 2.47 ± 0.18 $\mu\text{m/s}$; anti-N-MK, 3.32 ± 0.25 $\mu\text{m/s}$). (h) Number of adherent leukocytes per mm^2 (isotype control, 490.6 ± 48.8 cells/ mm^2 ; anti-N-MK, 259.8 ± 51.2 cells/ mm^2). (i) Hemodynamic parameters of investigated vessels. To determine P values, ANOVA on ranks with Dunn's multiple comparisons test was performed for b, d, and e, and an unpaired Student's *t* test was used for f–h. For all panels, *, $P < 0.05$; **, $P < 0.01$; ***, $P < 0.001$; n.s., not significant. Data are presented as mean \pm SEM or mean \pm individual data points.

MK promotes NET formation via LRP1

As the blockade of MK was able to reduce NET formation in the EAM model in vivo, we investigated whether MK was able to induce NET formation. Indeed, iMK substantially promoted forma-

tion of NETs of mPMNs in contrast to the unstimulated control (w/o) or after stimulation with soluble MK (sMK) as indicated by the presence of H3Cit (Fig. 6 a). We repeated these experiments with isolated human PMNs that were stimulated in the presence

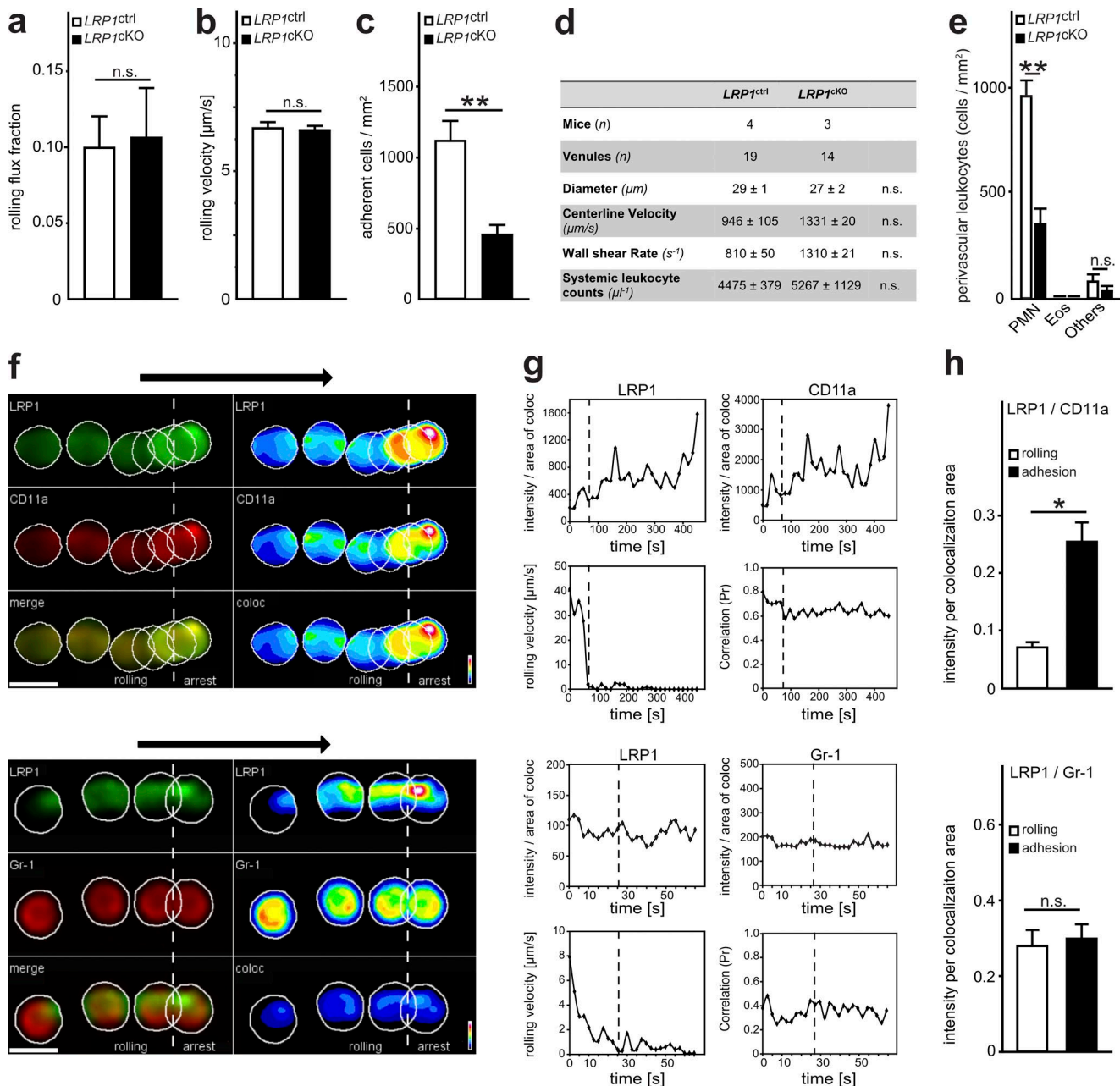


Figure 4. The MK receptor LRP1 is critical for leukocyte recruitment. (a–d) Intravital microscopy of cremaster muscle postcapillary venules of LRP1^{ctrl} and LRP1^{cko} mice 2 h after intrascrotal application of TNFα. *n* = 18 venules from four LRP1^{ctrl} mice, *n* = 14 venules from three LRP1^{cko} mice. (a) Leukocyte rolling flux fraction (LRP1^{ctrl}, 0.097 ± 0.020 [%]; LRP1^{cko}, 0.104 ± 0.032 [%]). (b) Leukocyte rolling velocity including 79 cells from four LRP1^{ctrl} mice and 71 cells from three LRP1^{cko} mice (LRP1^{ctrl}, 6.74 ± 0.24 μm/s; LRP1^{cko}, 6.66 ± 0.17 μm/s). (c) Number of adherent leukocytes per mm² (LRP1^{ctrl}, 1122.2 ± 133.2 cells/mm²; LRP1^{cko}, 456.0 ± 60.6 cells/mm²). (d) Hemodynamic parameters of investigated vessels. (e) Differential cell counts of perivascular leukocytes as analyzed histologically in cremaster muscle whole mounts after Giemsa staining 2 h after intrascrotal application of TNFα. Eos, eosinophils; Others, lymphocytes, basophils and monocytes; *n* = 47 venules from four LRP1^{ctrl} mice, *n* = 28 from three LRP1^{cko} mice (PMN: LRP1^{ctrl}, 958.3 ± 75.2 cells/mm², LRP1^{cko}, 354.1 ± 65 cells/mm²). (f–h) Flow chamber assays with mPMN using spinning disk confocal microscopy after coating with P-selectin, ICAM-1, and CXCL1. (f) The intensity of LRP1 and CD11a as well as LRP1 and Gr-1 expression together with the merged (merge) or colocalized (coloc) intensity of one single representative cell is depicted during rolling and adhesion. Arrows indicate direction of flow. Right panels demonstrate the intensity of LRP1 and CD11a cell surface expression using pseudocolors (heat map). (g) Analysis of the intensity per area of colocalization of LRP1 or CD11a as well as of LRP1 and Gr-1, kinetics of rolling velocity and correlation of colocalization during rolling and adhesion of one representative cell. (h) Mean intensity per area of colocalization of LRP1 and CD11a (rolling, 0.071 ± 0.009 arbitrary units [a.u.]; adhesion, 0.255 ± 0.033 a.u.) as well as of LRP1 and Gr-1 (rolling, 0.280 ± 0.042 a.u.; adhesion, 0.299 ± 0.037 a.u.) during rolling and adhesion. LRP1/CD11a: *n* = 23 cells/five experiments, LRP1/Gr-1: *n* = 11 cells/three experiments. To determine P values, an unpaired Student's *t* test was performed for a–c and h, and ANOVA on ranks with Dunn's multiple comparisons test was used for e. For all panels, *, *P* < 0.05; **, *P* < 0.01; n.s., not significant. Data are presented as mean ± SEM.

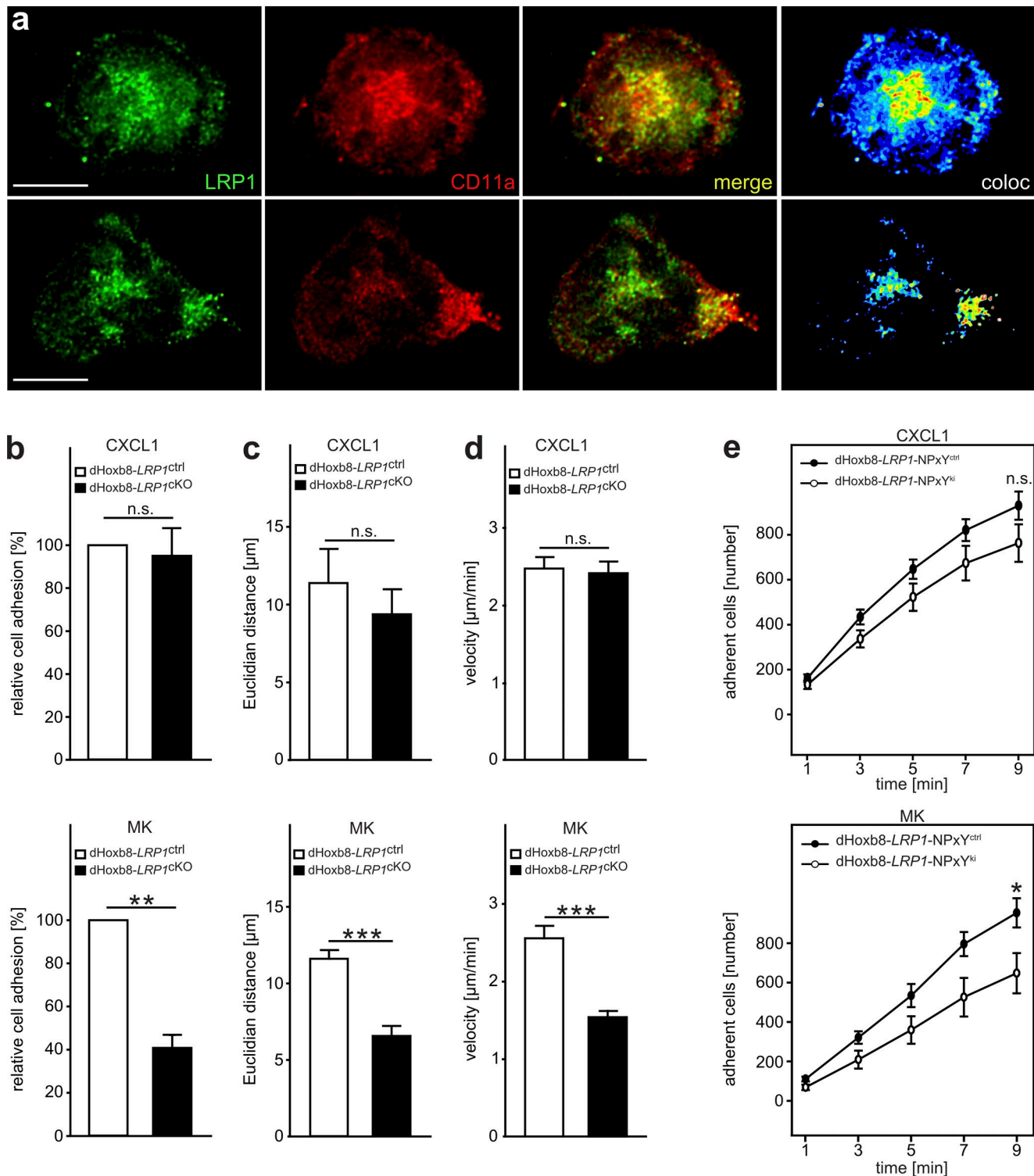


Figure 5. LRP1-mediated PMN recruitment is MK dependent. (a) Representative images of dHoxb8-*LRP1*^{ctrl} cells on microflow chambers coated with recombinant P-selectin, ICAM-1, and MK. Cells were perfused through chambers with a shear rate of 1 dyne/cm². Staining of cells was conducted using specific anti-LRP1 and anti-CD11a Abs, and imaging was performed using STED nanoscopy. Images show expression of LRP1 (green), CD11a (red), merge (yellow), and colocalization (coloc; pseudocolors [heat map]) of LRP1 and CD11a. The top panel illustrates an adherent cell and the lower panel a migrating cell. (b) Induction of adhesion of dHoxb8-*LRP1*^{ctrl} and dHoxb8-*LRP1*^{KO} cells under flow conditions (1 dyne/cm²) in microflow chambers coated with immobilized P-selectin, ICAM-1, and CXCL1 (dHoxb8-*LRP1*^{ctrl}, 100.0 [%]; dHoxb8-*LRP1*^{KO}, 95.1 ± 12.7 [%]) or MK (dHoxb8-*LRP1*^{ctrl}, 100.0 [%]; dHoxb8-*LRP1*^{KO}, 40.8 ± 6.0 [%]) as indicated. *n* = 4. (c and d) Migration of dHoxb8 cells under flow conditions. Euclidean distance (c; CXCL1: dHoxb8-*LRP1*^{ctrl}, 11.4 ± 2.2 μm; dHoxb8-*LRP1*^{KO}, 9.4 ± 1.6 μm; MK: dHoxb8-*LRP1*^{ctrl}, 11.6 ± 0.55 μm; dHoxb8-*LRP1*^{KO}, 6.56 ± 0.65 μm) as well as migration velocity (d; CXCL1: dHoxb8-*LRP1*^{ctrl}, 2.47 ± 0.25 μm/min; dHoxb8-*LRP1*^{KO}, 2.41 ± 0.26 μm/min; MK: dHoxb8-*LRP1*^{ctrl}, 2.56 ± 0.16 μm/min; dHoxb8-*LRP1*^{KO}, 1.54 ± 0.08 μm/min) of dHoxb8-*LRP1*^{ctrl} (white bar) and dHoxb8-*LRP1*^{KO} (black bar) under flow conditions (1 dyne/cm²). Flow chambers were coated with P-selectin, ICAM-1, and CXCL1 or MK as indicated. dHoxb8-*LRP1*^{ctrl} cells on CXCL1: *n* = 3 experiments/214 cells; dHoxb8-*LRP1*^{KO} cells on CXCL1: *n* = 3 experiments/303 cells. dHoxb8-*LRP1*^{ctrl} cells on MK: *n* = 4

of sMK, iMK, or PMA or left untreated for control (w/o). In contrast to sMK or the unstimulated control, we observed substantial NET formation in the presence of iMK and PMA (Fig. 6 b), as indicated by the colocalization of DNA and MPO. To elucidate whether LRP1 was involved in MK-mediated NETosis, we studied NET formation in the presence of MK using dHoxb8-*LRP1*^{ctrl} or dHoxb8-*LRP1*^{CKO} cells (Fig. 6 c). PMA induced NET formation regardless of the presence of LRP1, whereas almost no NET formation was observed in the negative control. We also found NET formation in dHoxb8-*LRP1*^{ctrl} cells on iMK. However, NET formation was significantly reduced in dHoxb8-*LRP1*^{CKO} cells compared with dHoxb8-*LRP1*^{ctrl} cells in the presence of iMK (Fig. 6 d), suggesting that MK promotes NET formation via LRP1.

Discussion

In the past three decades, research on the pathogenesis of myocarditis has been focused on the impact of adaptive immunity, whereas the role of PMNs as classical drivers of innate immunity has only been marginally addressed. Here, we demonstrate the presence of NETs in EMBs of patients with active myocarditis. To our knowledge, this is the first description of NETs in human myocardial tissue.

Although initial triggers differ in human myocarditis compared with EAM, sustained inflammation of the myocardium by a subsequent autoimmune response mediated by CD4⁺ T cells generally represents the common feature of chronic myocarditis regardless of the trigger (Rose, 2014). The fact that depletion of CD4⁺ T cells completely prevented EAM in mice (Smith and Allen, 1991) led to the concept that myocarditis is a T cell-mediated disease (Afanasyeva et al., 2004b). We found that disease severity could be substantially reduced by targeting NETs, suggesting a putative connection between the T cell response and NETosis. Indeed, a direct link of NETs and CD4⁺ T cells has been demonstrated as NETs were able to reduce the threshold for CD4⁺ T cell activation (Tillack et al., 2012). This interplay may explain that blocking either NETs or CD4⁺ T cells profoundly diminished cardiac inflammation in EAM (Afanasyeva et al., 2001, 2004a,b).

In our study, blockade of the cytokine MK substantially reduced PMN infiltration into the inflamed cardiac tissue in EAM. This is in line with our previous findings in the inflamed cremaster muscle, where diminished leukocyte adhesion and subsequent infiltration were observed in MK-deficient mice (Weckbach et al., 2014). Surprisingly, in the EAM model, not only the absolute number of NET⁺ PMNs was reduced after inhibition of MK but also the relative number of NET⁺ PMNs as a percentage of all extravasated PMNs. These findings may point to a dual function of MK by promoting the recruitment of PMNs as well as the formation of NETs. Indeed, MK was able to induce NETosis of isolated human and murine PMNs as well as dHoxb8 cells in vitro.

In accordance with our previous work, showing that immobilization of MK was required to mediate PMN adhesion (Weckbach et al., 2014), only iMK, but not sMK, was able to induce NETosis. Whether this is due to orientation of the MK molecule, for example, or a matter of protein clustering remains elusive.

MK consists of two domains, a C-terminal and an N-terminal domain, which exert different functions (Muramatsu, 2014). The fact that the Ab directed against the N-terminal domain of MK, but not the Ab directed against the C-terminal domain, blocked leukocyte infiltration in EAM suggests that the N-terminal domain is specifically required for the observed effects. Accordingly, the N-terminal domain has been shown to be particularly relevant for the stabilization of the protein via dimerization (Kojima et al., 1997; Muramatsu, 2014). This could potentially explain why the anti-N-MK Ab, but not the anti-C-MK Ab, inhibited leukocyte infiltration in EAM. Another possible explanation is the blockade of the specific interaction of the proposed receptor LRP1 with the N-terminal MK domain by the anti-N-MK Ab. However, to our knowledge, at this point, it is still unclear which MK domain binds LRP1.

The exact mechanism by which MK promotes the recruitment of PMNs and NETosis during myocarditis in vivo remains partially unclear. There is evidence that MK binds to the glycocalyx of the endothelium via its heparin-binding sites in vivo (Novotny et al., 1993). Inflammatory conditions such as hypoxia lead to up-regulation and release of MK from endothelial cells (Weckbach et al., 2012). Increased expression and presentation of iMK on the endothelial surface interacting with PMNs may therefore promote their infiltration during myocarditis. Due to a delay between the initial trigger and development of NETs from minutes to hours, depending on the stimulus (Jorch and Kubes, 2017), PMNs may undergo MK-mediated NETosis after infiltration in the cardiac tissue. Although MK was able to mediate NET formation in vitro, a contribution of other proinflammatory mediators to NET formation is possible in the complex scenario of the inflamed heart. Moreover, blocking MK not only reduced PMN but also reduced CD4⁺ T cell infiltration. Whether the reduction of PMN/NETs subsequently resulted in decreased CD4⁺ T cell recruitment in our model or whether MK directly mediated the recruitment of CD4⁺ T cells remains unclear and requires further investigation. In fact, we found expression of MK in the perivascular compartment of the inflamed cardiac tissue, supporting the idea of a direct involvement of MK in the leukocyte recruitment process (Stark et al., 2013). However, the exact source and localization of MK in vivo under steady state and inflammatory conditions need to be clarified in further studies.

In a mouse model of ascending aortic constriction mimicking aortic stenosis and leading to pressure overload-mediated heart dysfunction, NETs acted as major drivers of cardiac fibrosis (Martinod et al., 2017). Accordingly, collagen deposition was

experiments/280 cells; dHoxb8-*LRP1*^{CKO} cells on MK: $n = 4$ experiments/197 cells. (e) Induction of adhesion of dHoxb8-*LRP1*-NPxY^{ctrl} and dHoxb8-*LRP1*-NPxY^{ki} cells under flow conditions (1 dyne/cm²) in microflow chambers coated with immobilized P-selectin, ICAM-1, and CXCL1 (top diagram; dHoxb8-*LRP1*-NPxY^{ctrl}, 929.9 ± 62.9 cells; dHoxb8-*LRP1*-NPxY^{ki}, 762.8 ± 83.7 cells) or MK (bottom diagram; dHoxb8-*LRP1*-NPxY^{ctrl}, 953.3 ± 74.2 cells; dHoxb8-*LRP1*-NPxY^{ki}, 647.3 ± 101.8 cells). $n = 6$. To determine P values, an unpaired Student's *t* test was performed. For all panels, *, $P < 0.05$; **, $P < 0.01$; ***, $P < 0.001$; n.s., not significant. Data are presented as mean \pm SEM.

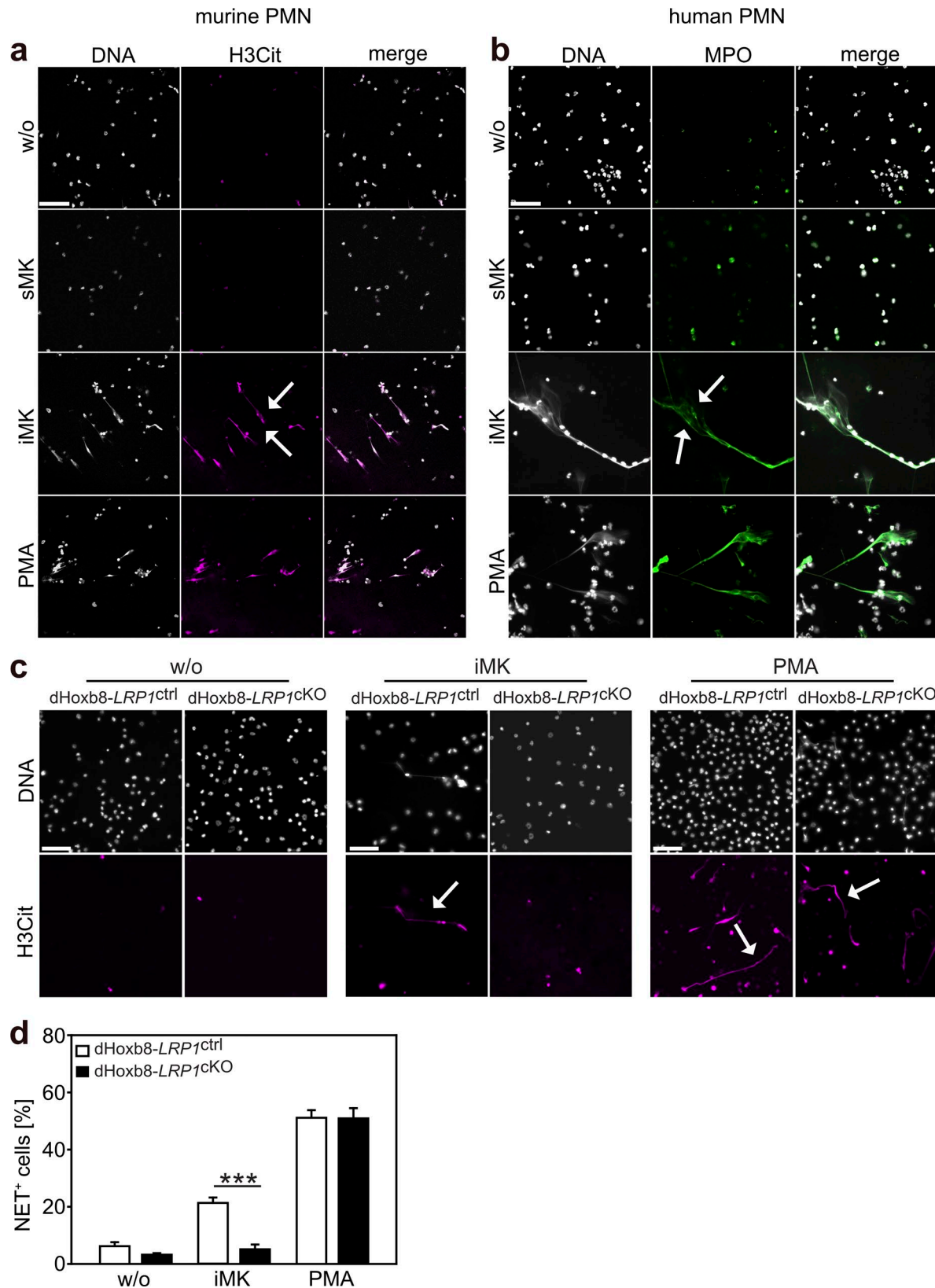


Figure 6. MK induces NET formation via LRP1. (a) Representative immunofluorescence images of BM-derived isolated mPMN. Cells were exposed to sMK, iMK, PMA or left untreated for control (w/o) on murine fibrinogen for 16 h. DNA (white) and H3Cit (magenta). Arrows indicate NETs. Bar, 40 μ m. $n = 3$. (b) Images of human PMNs freshly isolated from healthy donors. Cells were stimulated in the presence of human fibrinogen with sMK, iMK, or PMA or left unstimulated for control (w/o). Staining for DNA (white) and MPO (green) was subsequently conducted. $n = 3$. (c) Representative immunofluorescence images of dHoxb8-LRP1^{ctrl} or dHoxb8-LRP1^{cKO} cells. Cells were stimulated in the presence of iMK, PMA, or left unstimulated for control (w/o). Staining for DNA (white) and H3Cit (magenta) is depicted as indicated. Bar, 40 μ m. $n = 3$. (d) Quantitative analysis of NET formation of dHoxb8-LRP1^{ctrl} or dHoxb8-LRP1^{cKO} in the presence

markedly reduced and systolic function was preserved in PAD4^{-/-} mice or after administration of DNase in this model. In our study, we observed reduced fibrosis after blocking MK. The fact that neutralizing MK during the acute phase of myocarditis mainly impaired PMN and CD4⁺ T cell infiltration as well as NETosis supports the idea that PMNs forming NETs are major drivers of cardiac fibrosis in this model. Whether MK fosters fibrosis directly or indirectly by promoting inflammation remains unclear. Interestingly, Zhang et al. (2015) demonstrated that a pathway involving Nox1, MK, Notch2, and the angiotensin-converting enzyme contributed to lung remodeling and fibrosis. However, a direct contribution of MK to cardiac fibrosis remains to be determined.

Our data indicate a detrimental role of MK in cardiac inflammation. In contrast, animal models of myocardial infarction have shown a protective role of MK for the injured cardiac tissue by preventing apoptosis and mediating angiogenesis (Takenaka et al., 2009; Sumida et al., 2010). Here, PMN infiltration, although mostly considered to be detrimental (Epelman et al., 2015), may also have beneficial effects for post-myocardial infarction healing (e.g., by polarizing macrophages toward a reparative phenotype; Horckmans et al., 2017). Thus, MK may have a protective effect by mediating PMN recruitment in myocardial infarction models. Nonetheless, most studies investigating MK under chronic inflammatory conditions have clearly indicated a harmful role of MK for the host (Maruyama et al., 2004; Wang et al., 2008). Moreover, overexpression of MK promoted pressure overload-induced cardiac remodeling and cardiac dysfunction (Netsu et al., 2014). Thus, a beneficial or detrimental effect of MK during cardiac inflammation may depend on the mechanism of cardiac injury.

MK has been shown to function as ligand for LRP1 on different cell types (Lillis et al., 2008), and binding of MK to PMN was compromised after blocking LRP1 (Weckbach et al., 2014). Similar to the data in MK^{-/-} mice (Weckbach et al., 2014), leukocyte adhesion and extravasation were substantially diminished in the absence of LRP1 in our study, indicating that LRP1 is critically involved in mediating adhesion. Inhibiting LRP1 with RAP, which blocks all members of the LDL receptor family, reduced leukocyte infiltration during EAM. However, we cannot exclude that the blockade of LDL receptor family members other than LRP1 contributed to our findings. Whether MK acts by engaging LRP1 in vivo still needs to be determined. Other groups have shown that LRP1 was able to interact with the β_2 integrins LFA-1 and the macrophage-1 antigen (CD11b/CD18; Spijkers et al., 2005; Ranganathan et al., 2011), which are critical for adhesion, spreading, and intraluminal crawling of PMN during the recruitment process (Ley et al., 2007). Spijkers et al. (2005) demonstrated that LRP1 was important for adhesion of the monocyte-like cell line U937 on isolated endothelial cells under flow conditions by being involved in CD11a clustering. Accordingly, we found a clear colocalization and clustering of LRP1 and CD11a on PMN when

the cells became adherent, cumulating in a concentrated area of LRP1 and CD11a expression, which potentially represents the adhesion site where cells interacted with the adhesive substratum.

Whereas clustering and colocalization of LRP1 and CD11a were not dependent on MK but also occurred in the presence of CXCL1, adhesion of dHoxb8-LRP1^{CKO} cells was only compromised in the presence of MK. In contrast, CXCL1-induced adhesion did not rely on LRP1, suggesting that MK-mediated adhesion was LRP1 dependent. Accordingly, spreading and intraluminal crawling were diminished in dHoxb8-LRP1^{CKO} cells exposed to iMK, but not to immobilized CXCL1. These findings imply that MK is not required to initiate LFA-1 clustering but may enhance adhesion by β_2 integrins via LRP1. Here, the membrane distal NPxY domain of LRP1 seems to be involved in MK-mediated adhesion. Similar to PMN adhesion, MK-mediated NET formation was dependent on LRP1 in vitro, suggesting an important role of LRP1 for MK-mediated PMN functions.

In conclusion, our results identify a novel and important role of PMN and NETs in myocarditis. We provide evidence that NETs are detrimental for the host during myocarditis. In addition, we propose the model that the cytokine MK promotes PMN infiltration into the myocardium and may contribute to NET formation via LRP1 in this context. To date, there is no established therapy for patients with chronic inflammatory cardiomyopathy other than nonspecific immunosuppression with limited benefits and severe side effects. Therefore, blocking MK or NETs could represent novel and promising therapeutic options for patients with myocarditis.

Materials and methods

Human samples

The study was conducted according to the Declaration of Helsinki and approved by the Ethics Committee of the University of Munich. Human whole blood was drawn from healthy volunteers. Paraffin-embedded EMBs from patients with myocarditis were retrospectively analyzed. Clinical data of patients were obtained from medical records. The necessity for informed consent was waived by the local ethics committee due to the retrospective nature of the study.

Mice

LRP1^{fl/fl} mice on a 129S7/SvEvBrd genetic background were obtained from The Jackson Laboratory. LRP1^{fl/fl} mice were crossed with vav1-cre mice maintained on a C57Bl/6 background to generate LRP1^{fl/fl}/vav-cre⁺ (LRP1^{CKO}) and LRP1^{fl/fl}/vav-cre⁻ (LRP1^{ctrl}) animals as controls. For experiments, only littermates were used as controls. For the EAM model, 8-wk-old male WT mice on a BALB/c background were purchased from Charles River. CD4⁺ T cell proliferation assays were conducted in 8-wk-old BALB/c WT mice. For the cremaster muscle model using the anti-N-MK

of iMK (dHoxb8-LRP1^{ctrl}, 21.3 ± 1.9 NET⁺ cells [%]; dHoxb8-LRP1^{CKO}, 5.12 ± 1.7 NET⁺ cells [%]), PMA (dHoxb8-LRP1^{ctrl}, 51.1 ± 2.7 NET⁺ cells [%]; dHoxb8-LRP1^{CKO}, 50.9 ± 3.6 NET⁺ cells [%]), or without simulation (dHoxb8-LRP1^{ctrl}, 6.2 ± 1.4 NET⁺ cells [%]; dHoxb8-LRP1^{CKO}, 3.2 ± 0.6 NET⁺ cells [%]). Data show the number of NET⁺ cells as a percentage of all dHoxb8 cells. *n* = 3. To determine P values, one-way ANOVA with Holm-Sidak multiple comparisons test was performed. ***, *P* < 0.001. Data are presented as mean ± SEM.

blocking Ab, 8–12-wk-old C57Bl/6 WT mice were used. Animals were fed a standard chow diet ad libitum with free access to water. All animal experiments were institutionally approved by the Regierung von Oberbayern, Germany.

Isolation of human PMNs

Isolation was performed with a discontinuous isotonic Percoll gradient as previously described (Willeke et al., 2000). Human PMNs were subsequently resuspended in adhesion medium (HBSS; L0605; Biowest) supplemented with 20 mM Hepes (9105; Roth), 0.25% BSA (9306; Sigma-Aldrich), 0.1% glucose (7509; Roth), 1.2 mM Ca^{2+} (CN93; Roth), and 1 mM Mg^{2+} (9453; Roth). Human PMN viability as evaluated by a trypan blue exclusion test was >99%.

Isolation of murine PMNs

PMNs were isolated from murine BM of *LRP1^{ctrl}* and *LRP1^{KO}* mice using a discontinuous Percoll gradient as described previously (Pick et al., 2017). Isolated PMNs were cultivated for 24 h in RPMI 1640 medium (R8758; Sigma-Aldrich), supplemented with 20% WEHI-3B-conditioned medium at 37°C and 5% CO_2 . Murine PMN viability as evaluated by a trypan blue exclusion test was >95%.

Generation of Hoxb8-SCF cells

Hoxb8-SCF cells (referred to as Hoxb8 cells) were generated and differentiated toward PMNs as previously described (Wang et al., 2006; Redecke et al., 2013). HEK293T cells were transfected with the retroviral backbone pMSCVneo-ER-Hoxb8 and the ecotropic packaging vector pCL-Eco by Lipofectamine 2000 (116688; Thermo Fisher). The plasmids were a gift from Hans Häcker (St. Jude Children's Research Hospital, Memphis, TN). After 48 h, virus was harvested. BM cells of 8–10-wk-old mice were isolated, and progenitor cells were enriched by centrifugation over a HIS TOPAQUE 1083 (10831; Sigma-Aldrich) gradient. Progenitor cells were stimulated to proliferate in stem cell medium (RPMI 1640 plus 15% FCS [F2442; Sigma-Aldrich]; 1% penicillin/streptomycin [P4333, Merck]; 10 ng/ml murine IL-3 [213–13; Peprotech]; 20 ng/ml murine IL-6 [216–16; Peprotech]; and 2% SCF containing supernatant) for 3 d. For the generation of Hoxb8 cells, stimulated progenitor cells were transduced with the retrovirus by spinoculation with Lipofectamine (116688; Thermo Fisher) at 1,500 g for 80 min in progenitor outgrowth medium containing 1 μM β -estradiol (2758; Sigma-Aldrich), 30 μM β -mercaptoethanol (A1108; PanReac AppliChem), and 2% SCF containing supernatant. Every 3 d, cells were split into fresh progenitor outgrowth medium. After 4 wk, a Hoxb8 cell line was established. For differentiation of Hoxb8 cells toward PMN, 2.5×10^5 cells were washed in PBS with 1% FCS and taken up in differentiation medium (RPMI 1640 plus 10% FCS, 1% penicillin/streptomycin, 20 ng/ml murine G-CSF [250–05; Peprotech]; 2% SCF-containing supernatant, 30 μM β -mercaptoethanol) and allowed to differentiate for 4 d. Hoxb8 cells were generated from the BM of *LRP1^{KO}* and *LRP1-NP \times Y^{Ki}* mice as well as their matching controls.

EAM model

For induction of EAM, the purified synthetic peptide of cardiac α myosin heavy chain (Ac-RSLKLMATLFSTYASADR) emulsi-

fied in CFA (F5881; Sigma-Aldrich) was administered s.c. (200 μg of cardiac peptide per mouse) at day 1 and day 7. For sham controls, equal volumes of CFA and PBS were injected. To block MK, a mouse anti-human N-MK Ab (clone IP10, Cellmid; isotype: mouse IgG1, 401407, RRID:AB_11148722; BioLegend) or a mouse anti-human C-MK Ab (clone IP14, Cellmid; isotype: mouse IgG2a, 400264, RRID:AB_11148947; BioLegend) were applied i.p. (10 $\mu\text{g}/\text{g}$ body weight) twice a week until day 21. To investigate the role of NET formation during EAM, mice were treated with DNase (50 μg i.p. per mouse twice daily, Dornase α ; Roche) or Cl-amid (250 μg N- α -benzoyl-N5-(2-chloro-1-iminoethyl)-L-ornithine amide) s.c. per mouse daily (506282; Merck) from day 1 until day 21. Accordingly, sham controls and vehicle controls were treated with PBS. To study the impact of LRP1 on leukocyte infiltration, we implanted miniosmotic pumps (model 2004; Alzet) s.c., which were filled with chemically modified stable RAP (Prasad et al., 2015). Lyophilized RAP dissolved in PBS at a concentration of 112 μM or PBS as a control were released from miniosmotic pumps at a constant rate (0.25 $\mu\text{l}/\text{h}$), achieving RAP plasma levels of 5–10 nM (Strickland, D., personal communication). On day 21, mice were sacrificed and hearts were harvested for analysis.

Histology and heart/body weight ratio

For histopathological evaluation of cardiac tissue, mouse hearts were rinsed with PBS and fixed in PFA 4% (CP10; Roth) for at least 24 h. For analysis of the heart/body weight ratio, the pericardium, connective tissue, and vascular remains were excised carefully before hearts were weighed using a microbalance (CP64-OCE; Sartorius). Subsequently, hearts were dehydrated in a graded series of ethanol concentrations. Thereafter, tissues were embedded in paraffin (1.07158; Sigma-Aldrich). Murine sections were stained with hematoxylin (T865.1; Roth) and eosin (X883.1, day 21; Roth) to evaluate infiltration of hematopoietic cells or with Masson's trichrome (010802, day 63; Bio-Optica) to assess cardiac fibrosis. Acute infiltration was evaluated semi-quantitatively using an EAM score (0, no inflammatory infiltrates; 1, small foci of <100 inflammatory cells between myocytes; 2, larger foci of >100 inflammatory cells; 3, >10% of a cross section shows infiltration of inflammatory cells; 4, >30% of a cross section shows infiltration of inflammatory cells) as previously described (Valaperti et al., 2008). To assess fibrosis by morphometric evaluation, ~30 fields per section were chosen randomly. Fibrosis was evaluated using a semiquantitative score (0, 0–1%; 1, 1–2%; 2, 2–3%; 3, 3–4%; 4, 4–5%; 5, >5% fibrosis). All analyses were performed in a blinded manner.

Echocardiography

Transthoracic echocardiography was conducted using a Vevo2100 imaging system (VisualSonics) with a 40-MHz transducer at day 63. Anesthesia was performed with 2% isoflurane. To ensure a stable body temperature of 35.5–36.5°C, mice were transferred to a heated platform. Parasternal long-axis M-mode was used to standardize midventricular transducer positioning for short-axis M-mode imaging as previously described (Grabmaier et al., 2014). For evaluation of cardiac function, three consecutive cycles were measured and averaged.

NET induction

For NETosis experiments, *in vitro* 8-well slides (IBIDI) were coated with human or murine fibrinogen (100 µg/ml; IFIB; Dunn) or human or murine MK (20 µg/ml; 450-16; Peprotech) for 12 h at 4°C before the experiment. After washing wells with PBS, 3×10^5 PMNs suspended in adhesion medium (HBSS supplemented with 20 mM Hepes, 0.25% BSA, 0.1% glucose, 1.2 mM Ca^{2+} , and 1.0 mM Mg^{2+}) were added. Human PMNs were incubated and stimulated for 1 h, whereas mPMNs or Hoxb8 cells were stimulated for 16 h at 37°C. PMNs or Hoxb8 cells were stimulated with PMA (100 nM) in the presence of fibrinogen as a positive control.

Laser scanning confocal microscopy

To study NET formation *in vitro*, adherent PMNs were fixed with PFA 4% for 10 min. After blocking (PBS, goat serum 10%; G9023, BSA 1%; Sigma-Aldrich) for 2 h, primary Abs were added (human: rabbit-anti-human MPO Ab, clone SP72, ab93665; Abcam; murine: rabbit anti-mouse H3Cit Ab, polyclonal, ab5103; Abcam; rat-anti-mouse NE/mELA2 Ab: clone 887105, MAB4517; R&D Systems) and incubated for 90 min at room temperature (RT) in the dark. Subsequently, samples were washed and incubated with secondary Abs for 30 min (human: Alexa Fluor 488-conjugated goat-anti-mouse Ab, A21042; Thermo Fisher; murine: Alexa Fluor 488-conjugated goat anti-rat Ab, A11006; Thermo Fisher; and Alexa Fluor 546 goat anti-rabbit Ab, A11035; Abcam). Nuclear staining was performed using Hoechst 33342 (624249; Thermo Fisher) diluted 1:1,000 in human and murine experiments. Finally, samples were embedded using fluorescence mounting medium (S3023; DAKO). To quantify NET formation, the number of NET⁺ dHoxb8 cells as a percentage of all dHoxb8 cells per visual field was calculated. For each experiment, five fields per sample were randomly imaged and analyzed offline in a blinded manner. Confocal microscopy was conducted using a Leica SP8X WLL upright confocal microscope equipped with a 40×/1.3 NA oil immersion objective. Alexa Fluor 488 and Alexa Fluor 546 were recorded with hybrid photo detectors and Hoechst with a conventional multiplier tube. Images were analyzed offline using LAS X software (Leica) and ImageJ (National Institutes of Health).

To analyze NET formation in murine heart sections, samples were deparaffinized, rehydrated, and incubated in citrate buffer (1.5 mM citrate monohydrate [5110; Roth]; and 8.5 mM sodium citrate dihydrate [4088; Roth], adjusted to pH 6.0) at 100°C for 7 min for antigen retrieval. Subsequently, sections were left in citrate buffer at RT to cool below 30°C. To prevent nonspecific binding, sections were surrounded with PAP pen (S2002; DAKO) and incubated with blocking solution (PBS, goat serum 10%, BSA 1%, saponin 0.5% [47036; Sigma-Aldrich]) for 90 min at RT. Primary Abs (rat anti-mouse NE Ab, clone 887105 [MAB4517; R&D Systems]; rabbit anti-mouse H3Cit Ab, polyclonal [ab5103; Abcam]) were diluted 1:200 in blocking solution and incubated with the samples for 2 h at RT. After washing, sections were incubated with secondary Abs (Alexa Fluor 488-conjugated goat-anti-rat Ab [ab150157; Abcam]; Alexa Fluor 594-conjugated goat-anti-rabbit Ab [A11012; Thermo Fisher]) for 30 min at RT. For nuclear staining, Hoechst 33342 (624249; Thermo Fisher)

was diluted 1:1,000 together with secondary Abs in PBS/BSA 1% solution. Thereafter, samples were embedded using fluorescence mounting medium (S3023; DAKO). Confocal microscopy was conducted using a Leica SP8X WLL upright confocal microscope equipped with a 40×/1.3 NA oil-immersion objective. Alexa Fluor 488 and Alexa Fluor 594 were recorded with hybrid photo detectors and Hoechst with a conventional multiplier tube. Images were analyzed offline using LAS X software (Leica) and ImageJ (National Institutes of Health).

To study MK and CD31 expression in murine cardiac sections, 5-µm sections were deparaffinized, rehydrated, and incubated in antigen retrieval buffer (10 mM Tris-HCl, 2 mM EDTA, and 10% glycerol, pH 9.0) at 110°C for 18 min. Thereafter, slides were allowed to cool at RT for 30 min, followed by a PBS rinse. Tissue sections were surrounded by a hydrophobic barrier using PAP pen and blocked for 10 min with 2.5% goat serum. Incubation with the primary Abs (rabbit anti-human MK Ab, clone EP1143Y [ab52637; Abcam]; rabbit anti-mouse CD31 Ab, clone D8V9E, [77699; Cell Signaling]) was performed on a shaker for 1 h at RT. Slides were washed in PBSt (0.05% Tween + 2 mM EDTA) before adding secondary Abs (ImmPRESS HRP-conjugated goat anti-rabbit; MP-7401; Vector Laboratories). Sections were incubated with secondary Abs for 30 min on a shaker followed by one PBSt (0.2% Tween + 2 mM EDTA) and two PBSt (0.05% Tween + 2 mM EDTA) washes. Sections were subsequently incubated with tyramide signal amplification substrates. For multiplex staining, Ab stripping was performed in 10 mM citrate buffer (pH 6.2, 10% glycerol) in a pressure cooker at 110°C for 2 min before probing with the next primary Ab. To reduce red blood cell autofluorescence, slides were incubated at the end in TrueBlack Lipofuscin Autofluorescence Quencher (23007; Biotium; diluted 500-fold in 70% ethanol) for 30 s. Following a DAPI counterstain, slides were coverslipped using Prolong Gold Antifade Mountant (P36930; Thermo Fisher). Slides were scanned with a 40×/NA 0.95 objective (Zeiss) using the Zeiss AxioScan.Z1 (Whole Brain Microscopy Facility, University of Texas Southwestern Medical Center). DAPI, Alexa Fluor 488 (for OPAL520), Alexa Fluor 555 (for OPAL570), and Alexa Fluor 660 (for OPAL 690) channels were used to acquire images. The exposure time for image acquisition was between 5 and 100 ms. Images were prepared using Zen Lite (Zeiss).

To study NETosis in human cardiac biopsies, sections were incubated in HIER buffer (retriever-universal buffer, pH 7, 10 × [Aptum APO 0530500]) at 45°C for 90 min. After antigen retrieval, sections were left in the HIER buffer at RT to cool below 30°C, rinsed with deionized water three times and once with Tris-buffered saline (TBS), pH 7.4, and permeabilized for 5 min with 0.5% Triton X-100 in TBS, followed by three rinsing steps with TBS. Sections were surrounded with PAP pen and treated with blocking buffer for 30 min to prevent nonspecific binding. Primary Abs (rabbit anti-human H3Cit [ab5103; Abcam]; goat anti-human MPO [AF3667; R&D Systems]; and F(ab) Alexa Fluor 633-conjugated mouse anti-H2A-H2B-DNA complex, provided by Prof. Marc Monestier, Temple University School of Medicine, Philadelphia, PA) were diluted in blocking buffer and incubated over night at 37°C. As secondary Abs, the Cy3-conjugated donkey anti-rabbit Ab (711-165-152; Dianova) and the Alexa Fluor 488-

conjugated donkey anti-goat Ab (705–546-147; Dianova) were used. TBS supplemented with 1% BSA/2% donkey serum/5% cold water fish gelatin/0.05% Tween/0.05% Triton X-100 served as dilution and blocking buffer. Sections were mounted using Mowiol mounting medium (81381; Sigma-Aldrich) and screened for the presence of PMN using an Axioscan.Z1 slide scanner (Zeiss). Images of PMN-rich tissue areas were taken with a Leica TCS-SP8 confocal microscope equipped with a 63×/1.3 NA glycerol immersion objective. Recording was conducted using hybrid photo detectors and conventional multiplier tubes. Images were analyzed offline using LAS AF software (Leica) and ImageJ (National Institutes of Health).

STED nanoscopy

Microscopic inspection of the colocalization of LRP1 and CD11a *in vitro* was performed using STED nanoscopy. Isolated murine dHoxb8-LRP1^{ctrl} cells were stained with a rabbit anti-LRP1 Ab (clone EPR3724; ab195567; Abcam) and an Abberior STAR 635-conjugated goat anti-rabbit Ab (2-0012-002-7; Abberior) as well as a rat anti-mouse CD11a Ab (clone 2D7; 553118; BD) and an Alexa Fluor 594-conjugated donkey anti-rat Ab (A-21209, RRID: AB_2535795; Thermo Fisher). Stained cells were perfused through microflow chambers (μ -slides IV 0.1; IBIDI) coated with ICAM-1 (02203; Stemcell), P-selectin (737-PS; R&D Systems), and CXCL1 (250-11; Peprotech) as described below in detail. Imaging was conducted using an upright confocal microscope (Examiner, Zeiss) equipped with the confocal unit scanner CSU-X1 (Yokogawa Electric Corporation), a CCD camera (Evolve; Photometrics), and a 20×/1.0 NA water-immersion objective (Plan Apochromat; Zeiss). 20 min before the experiment, cells were stained with a FITC-labeled mouse anti-human LRP1 Ab (BioMac) as well as an allophycocyanin (APC)-labeled rat anti-mouse CD11a Ab (clone 2D7; 562810; BD) or an APC-labeled rat anti-mouse Gr-1 Ab (clone RB6-8C5; 108411, RRID: AB_313376; BioLegend). Images were obtained using two lasers with an excitation wavelength of 488 nm and 640 nm. 6.0.8 Software (3i) and Fiji/ImageJs plugin coloc2 (Daniel J. White, GE Healthcare, Aurora, OH) were used to analyze fluorescence intensities (I) and colocalization parameters (Pearson's correlation coefficient). Normalization of intensity values was calculated with following equation: $[I(t) - I(\text{min})]/[I(\text{max}) - I(\text{min})]$, where t = time point, min = minimal fluorescence intensity, and max = maximum fluorescence intensity. All analyses were performed in a blinded manner.

Intravital microscopy

Intravital microscopy was performed using LRP1^{ctrl} and LRP1^{ckO} mice as well as C57Bl/6 mice 2 h after intrascrotal injection of TNF α (500 ng per mouse) as previously described (Weckbach et al., 2014). For experiments with C57Bl/6 mice, anti-N-MK Ab (Cellmid) or the matching isotype control Ab (clone MOPC-21; 400101; BioLegend) were applied *i.p.* 12 h before the experiment. Briefly, after cannulation of the carotid artery, the cremaster muscle was surgically prepared as reported previously (Weckbach et al., 2014). Intravital microscopy was conducted using an upright microscope (Axiovert Vario, Zeiss; and DM6 FS, Leica) at 37°C and recorded using a digital camera (AxioCam HSm, Zeiss; and Zyla sCMOS, Andor Technology). Leukocyte counts were obtained from whole blood (ProCyt Dx; IDEXX Laboratories). Cells attached >30 s were defined as adherent. Diameter of postcapillary venules ranged from 20 to 40 μ m. Centerline red blood cell velocities in microvessels were analyzed using fluorescent microspheres (0.5 μ m diameter; Polysciences). Blood flow was calculated from the length of at least three microspheres measured in a snapshot image with a defined exposure time and converted offline to mean blood flow velocities. Wall shear rates were calculated as previously described (Weckbach et al., 2014).

Cremaster muscle whole mounts

To assess the number of extravasated leukocytes, cremaster muscles were exteriorized and surgically prepared 2 h after intrascrotal application of TNF α (500 ng; 315-01A; Peprotech) as previously reported (Weckbach et al., 2014). Tissues were fixed, stained with Giemsa, and mounted (AGAR Scientific). The number of perivascular leukocytes was analyzed using a Leica DM2500 microscope with a 100×/1.4 NA oil-immersion objective (HCX PLAPO). Images were obtained using a CMOS color camera (DMC2900 CMOS Sensor camera; Leica). Leukocyte subpopulations were differentiated morphologically.

Spinning disk confocal microscopy

To study cell surface expression of LRP1 and CD11a of rolling and adherent cells under flow conditions, spinning-disk confocal microscopy was conducted. Isolated mPMNs or dHoxb8-LRP1^{ctrl} cells were perfused through microflow chambers (μ -slides IV 0.1; IBIDI) coated with ICAM-1 (02203; Stemcell), P-selectin (737-PS; R&D Systems), and CXCL1 (250-11; Peprotech) as described below in detail. Imaging was conducted using an upright confocal microscope (Examiner, Zeiss) equipped with the confocal unit scanner CSU-X1 (Yokogawa Electric Corporation), a CCD camera (Evolve; Photometrics), and a 20×/1.0 NA water-immersion objective (Plan Apochromat; Zeiss). 20 min before the experiment, cells were stained with a FITC-labeled mouse anti-human LRP1 Ab (BioMac) as well as an allophycocyanin (APC)-labeled rat anti-mouse CD11a Ab (clone 2D7; 562810; BD) or an APC-labeled rat anti-mouse Gr-1 Ab (clone RB6-8C5; 108411, RRID: AB_313376; BioLegend). Images were obtained using two lasers with an excitation wavelength of 488 nm and 640 nm. 6.0.8 Software (3i) and Fiji/ImageJs plugin coloc2 (Daniel J. White, GE Healthcare, Aurora, OH) were used to analyze fluorescence intensities (I) and colocalization parameters (Pearson's correlation coefficient). Normalization of intensity values was calculated with following equation: $[I(t) - I(\text{min})]/[I(\text{max}) - I(\text{min})]$, where t = time point, min = minimal fluorescence intensity, and max = maximum fluorescence intensity. All analyses were performed in a blinded manner.

Functional analysis of dHoxb8 cells under flow conditions *in vitro*

dHoxb8-LRP1^{ckO} and dHoxb8-LRP1^{ctrl} cells were analyzed *in vitro* using microflow chambers (μ -slides IV 0.1; IBIDI). Coating with P-selectin, ICAM-1, and murine MK or CXCL1 was performed for 12 h at 4°C before the experiment. After blocking the flow chambers for 2 h at RT, dHoxb8-LRP1^{ckO} and dHoxb8-LRP1^{ctrl} cells were suspended in adhesion medium (HBSS supplemented with 20 mM Hepes, 0.25% BSA, 0.1% glucose, 1.2 mM Ca²⁺, and 1.0 mM Mg²⁺). Subsequently, dHoxb8 cells (7.5×10^5 cells/ml) were directly perfused through the flow chamber at constant shear stress (1 dyne/cm²) using a high-precision syringe pump (model KDS-232; KD Scientific). To study induction of adhesion, time-lapse videos were recorded from 18 different fields of view within the flow chamber at five different time points. Time-lapse video microscopy was performed using the Zeiss Axiovert 200M microscope equipped with a Plan-Apochromat 20×/0.75 NA objective, AxioCam HR digital camera, and temperature-con-

trolled environmental chamber at 37°C. The number of adherent dHoxb8 cells was determined for analysis of cell adhesion. For measurement of detachment under flow conditions, dHoxb8 cells were seeded into flow chambers. After 10 min of incubation at 37°C, shear stress was applied and gradually increased from 0.2 to 8.0 dyne/cm² every 90 s. Time-lapse videos were recorded for 9 min, and relative adhesion was calculated for seven time points as the percentage of adherent cells relative to initially adherent cells at 0.2 dyne/cm² (100%). The number of adherent cells was analyzed offline using ImageJ (National Institutes of Health). To analyze mechanotactic crawling of dHoxb8 cells, shear stress (1 dyne/cm²) was applied for 10 min. The cell velocity and the Euclidian distance traveled by migration were measured using ImageJ with the manual tracking plugin (Fabrice Cordelies, Institute Curie, Paris, France). Migration analysis software provided by IBIDI was used for single-cell migration tracks. Cell spreading was analyzed by measuring the cell area after 10 min of flow (1 dyne/cm²) using ImageJ.

Flow cytometry

Surface expression of CD11a, CD11b, and CD18 was measured on isolated mPMNs (2.5 × 10⁵/sample) from LRP1^{CKO} and LRP1^{ctrl} mice. PMNs were stimulated with recombinant murine TNFα for 20 min at 37°C or left unstimulated as a control. Cell staining was performed with the APC-conjugated rat anti-mouse CD11a Ab (clone 2D7 [BD]; isotype: rat IgG2a [400544, RRID:AB_11147167; BioLegend]), PE-conjugated rat anti-mouse CD11b Ab (clone M1/70 [RM2804; Thermo Fisher]; isotype: rat IgG2b [21275534; ImmunoTools]), and the FITC-conjugated rat anti-mouse CD18 Ab (clone C71/16 [553292; BD]; isotype: rat IgG2a [554688; BD]).

For analysis of myocardial leukocyte infiltration, flow cytometry was performed from hearts of EAM mice treated with either the mouse anti-human N-MK Ab (clone IP10 [Cellmid]; isotype: mouse IgG1 [92196; BioLegend]) or the mouse anti-human C-MK Ab (clone IP14 [Cellmid]; isotype: mouse IgG2a [92394; BioLegend]). To obtain single-cell suspensions, hearts were extracted and perfused with PBS. Next, hearts were cut in small pieces and incubated with Liberase (5401119001; Roche) for 45 min at 37°C. After incubation, the suspension was mixed gently, filtered through a 40-μm cell strainer, washed, and suspended in PBS. Cells were labeled with a FITC-conjugated rat anti-mouse CD11b Ab (clone M1-70; 553310; BD), PE-conjugated rat anti-mouse Gr-1 Ab (clone RB6-8C5, 108407, RRID:AB_313372; BioLegend), PE-conjugated rat anti-mouse Ly6G Ab (clone 1A8, 127607; BioLegend), peridinin-chlorophyll protein (PerCP)-conjugated rat anti-mouse CD45 Ab (clone 30F-11, 561047; BD), and Pacific Blue-conjugated rat anti-mouse CD4 Ab (clone RM4-5, 558107; BD) and incubated for 30 min at RT. Matching isotype Abs served as controls. Subsequently, cells were washed and resuspended in PBS supplemented with 1% BSA and immediately subjected to flow cytometry. All experiments were conducted using a Gallios flow cytometer (Beckman Coulter). Data were analyzed using FlowJo software (TreeStar).

RNA isolation and real-time PCR

Hearts of EAM or sham-treated control mice were removed, rinsed with PBS, and homogenized mechanically using an Ul-

tra-Turrax T8 homogenizer (IKA Labortechnik). RNA was isolated using TRIzol (15596026; Thermo Fisher) according to the manufacturer's protocol, and genomic DNA was digested using the DNase I Amplification Grade kit (18068015; Thermo Fisher). 1 μg total RNA was transcribed into cDNA using the Omniscript RT kit (205111; Qiagen). Quantitative PCR was conducted using SsoAdvanced Universal SYBR Green Supermix (1725271; Bio-Rad). Hypoxanthine-guanine phosphoribosyltransferase (HPRT) was used as reference gene. The following primers were used: MK (forward, 5'-GTCAATCAGCCTGTCTCT-3'; reverse, 5'-CAAGTATCAGGGTGGGGAGA-3'), HPRT (forward, 5'-ACAGGCCAGACTTTGTTGGAT-3'; reverse, 5'-ACTTGCCTCATCTTAGGCT-3'). Data are presented as relative expression of MK normalized to HPRT. Mean expression level of sham samples was defined as 1.

CD4⁺ T cell proliferation

CD4⁺ T cells were MACS-sorted from erythrocyte-lysed mouse splenocytes in accordance to the manufacturer's protocol (Miltenyi Biotec). Cells were labeled with 2.5 μM CFSE (C34554; Thermo Fisher) and activated with anti-CD3/CD28 beads (ratio 2:1; Miltenyi Biotec) in 96-well round-bottom plates at 20,000 cells per well. Cells were cultured for 3 d in RPMI 1640 medium supplemented with 10% FCS, penicillin/streptomycin, β-mercaptoethanol, and sodium pyruvate (8793; Roth), 20 ng/ml IL-2 (212-12; Peprotech), and nonessential amino acids (M7145; Sigma-Aldrich) at 37°C and 5% CO₂. Cell proliferation of the CD4⁺ cell population (APC-conjugated rat anti-mouse CD4 Ab, clone RM4-5 [553051; BD]) was analyzed with the LSRII Fortessa analyzer (BD) and FlowJo software (TreeStar).

ELISA

Mouse hearts of EAM mice treated with anti-N-MK or an isotype Ab for control were thoroughly rinsed with ice-cold PBS and weighed. The cardiac tissue was cut into small pieces and homogenized in lysis buffer (100 mM Tris, pH 7.4, 150 mM NaCl, 1 mM EGTA, 1 mM EDTA, 1% Triton X-100, 0.5% sodium deoxycholate, phosphatase, and protease inhibitor cocktail) mechanically using an Ultra-Turrax T8 homogenizer (IKA Labortechnik). Samples were subsequently centrifuged for 20 min at 5,000 g at 4°C, and the supernatant was used for ELISA. MIP2-α was quantified according to the manufacturer's protocol (USB-026622; US Biological). The absorbance was measured with a microtiter plate reader at 450 nm. For each sample, duplicates were analyzed. The intra-assay variation among the duplicates was <10%. The cytokine concentrations were calculated from the standard curves using linear regression analysis.

PCR

Genotyping PCR was performed with the thermocycler UNO II (Biometra), a Taq DNA polymerase (9PIM166; Promega), and specific primer sets (Metabion) according to standard procedures. The following primers were used: LRP1 (forward, 5'-CATACCCTCTTCAAACCCCTTCTCTG-3'; reverse, 5'-GCAAGCTCTCCTGCTCAGACCTGG-3'). Vav1-cre (forward, 5'-GCCTGCCCTCCC TGTGGATGCCACCT-3'; reverse, 5'-GTGGGCAGAAGGGGCAGC CACACCATT-3'). After amplification, electrophoretic separation was performed with a gel containing 1.5% agarose (3810; Roth)

and 0.002% ethidium bromide (HP46; Roth). Detection was performed with 366 nm UV light (Biometra).

SDS-PAGE and immunoblotting

Samples were incubated in lysis buffer containing 25 mM Tris-HCl, pH 7.5, 150 mM NaCl, 0.5 mM EDTA, 1% Triton X-100, and 1% Na-deoxycholate (D6750; Roth), 1 mM diisopropylfluorophosphate (D0879; Sigma-Aldrich), 100 μ M NaF (4503; Roth), and 200 μ M Na-orthovanadate (0735; Roth) supplemented with protease inhibitors (Sigma-Aldrich) for 30 min at 4°C and subsequently centrifuged at 13,000 g for 1 min. The supernatant was boiled for 5 min at 95°C with 2 \times Laemmli buffer. Proteins were separated using a 10% acrylamide SDS-PAGE gel and electrophoretically transferred to polyvinylidene difluoride membranes. After incubation with 5% milk in TBS with Tween 20 for 1 h, the following Abs were used: rabbit anti-LRP1 Ab (clone EPR3724; ab92544, RRID:AB_2234877; Abcam), goat anti-actin Ab (polyclonal; sc1616, RRID:AB_630836; Santa Cruz), peroxidase-conjugated goat anti-rabbit IgG Ab (A0554; Sigma-Aldrich), and peroxidase-conjugated rabbit anti-goat IgG Ab (401515; Calbiochem). For detection, a chemiluminescence kit (32106; Pierce) was used. Analysis was performed with a Hamamatsu 1394 ORCA-ERA camera, the Aequoria MDS Macroscopic Imaging System, and Wasabi software (Hamamatsu Photonics).

Statistical analysis

Data represent mean \pm SEM. Statistical significance ($P < 0.05$) was determined with Sigma Plot v10.0 (Systat Software) using a Student's *t* test, Mann-Whitney rank-sum test, or Kruskal-Wallis ANOVA or one-way ANOVA test.

Online supplemental material

Fig. S1 shows staining of DNA, NE, and H3cit in cardiac sections of EAM mice after targeting NETs with DNase. Fig. S2 demonstrates MK expression and function during EAM. Fig. S3 illustrates that IgG1 control Abs do not affect EAM. Fig. S4 exhibits that LRP1 is involved in leukocyte infiltration in vivo. Fig. S5 shows an important contribution of the MK-LRP1 axis for different PMN recruitment steps. Video 1 displays the systolic function after blocking MK in EAM mice using mouse echo. Video 2 demonstrates the impact of LRP1 on leukocyte rolling and adhesion in the inflamed mouse cremaster muscle in vivo. Video 3 illustrates the expression of LRP1 and CD11a. Video 4 shows the expression of LRP1 and Gr-1 in murine PMNs during rolling and adhesion in vitro. Video 5 shows the colocalization of LRP1 and CD11a in adherent dHoxb8 cells. Video 6 displays the role of LRP1 for MK-mediated crawling under flow conditions.

Acknowledgments

The authors thank Judith Arcifa and Severin Gylstorff for their excellent technical assistance as well as Dr. Steffen Dietzel (Core Facility Bioimaging, Biomedical Center, Ludwig-Maximilians-Universität Munich) for his help with confocal microscopy and STED nanoscopy. The authors also thank Prof. Reinhard Kandolf for providing human EMBs (Cardiopathology, Institute for Pathology and Neuropathology, University Hospital Tuebingen, Tuebingen,

Germany). The authors are grateful to Dr. Arturo Zychlinsky (Max Planck Institute for Infection Biology, Berlin, Germany) for his support and advice and for sharing expert knowledge on NETosis. The authors also thank Dr. Anton Roebroek for providing BM of LRP1 NPxYxxL knock-in as well as control mice. Anti-MK Abs were generously provided by Cellmid (Sydney, Australia).

This work was supported by the Deutsche Forschungsgemeinschaft (grant SFB 914, project A02 to B. Walzog, B02 to S. Massberg, and Z03 to B. Walzog; DFG KL 595/2-3 to K. Klingel), the FöFoLe (L.T. Weckbach and U. Grabmaier) and the LMU Excellence program of the Ludwig-Maximilians-University Munich (L.T. Weckbach and U. Grabmaier), the Deutsche Gesellschaft für Kardiologie (U. Grabmaier), and the National Institutes of Health (grants F31 CA19603301 to N. Sorrelle and R35 HL125743 to D.K. Strickland).

The authors declare no competing financial interests.

Author contributions: L.T. Weckbach and U. Grabmaier performed most of the experiments, designed the experiments, analyzed all the data, and wrote the manuscript. A. Uhl and F. Boehm conducted the myocarditis and NETosis experiments. S. Gess performed flow chamber experiments. A. Zehrer generated Hoxb8 cells. R. Pick designed and carried out the spinning-disk confocal microscopy and STED nanoscopy experiments. M. Salvermoser performed intravital microscopy. T. Czermak and J. Pircher helped design the NET stainings in vitro and in mouse tissue in vivo. N. Sorrelle performed immunofluorescence staining. M. Migliorini and D.K. Strickland produced RAP. K. Klingel provided endomyocardial biopsies of myocarditis patients. V. Brinkmann and U. Abu Abed conducted NET staining experiments in human myocardial biopsies. U. Eriksson conducted T cell proliferation experiments and analyzed the data. S. Massberg analyzed the data and wrote the manuscript. S. Brunner analyzed the data and designed experiments. B. Walzog designed experiments, analyzed the data, and wrote the manuscript.

Submitted: 12 June 2018

Revised: 21 October 2018

Accepted: 20 December 2018

References

- Afanasyeva, M., Y. Wang, Z. Kaya, S. Park, M.J. Zilliox, B.H. Schofield, S.L. Hill, and N.R. Rose. 2001. Experimental autoimmune myocarditis in A/J mice is an interleukin-4-dependent disease with a Th2 phenotype. *Am. J. Pathol.* 159:193–203. [https://doi.org/10.1016/S0002-9440\(10\)61685-9](https://doi.org/10.1016/S0002-9440(10)61685-9)
- Afanasyeva, M., D. Georgakopoulos, D.F. Belardi, A.C. Ramsundar, J.G. Barin, D.A. Kass, and N.R. Rose. 2004a. Quantitative analysis of myocardial inflammation by flow cytometry in murine autoimmune myocarditis: correlation with cardiac function. *Am. J. Pathol.* 164:807–815. [https://doi.org/10.1016/S0002-9440\(10\)63169-0](https://doi.org/10.1016/S0002-9440(10)63169-0)
- Afanasyeva, M., D. Georgakopoulos, and N.R. Rose. 2004b. Autoimmune myocarditis: cellular mediators of cardiac dysfunction. *Autoimmun. Rev.* 3:476–486. <https://doi.org/10.1016/j.autrev.2004.08.009>
- Brinkmann, V., U. Reichard, C. Goosmann, B. Fauler, Y. Uhlemann, D.S. Weiss, Y. Weinrauch, and A. Zychlinsky. 2004. Neutrophil extracellular traps kill bacteria. *Science*. 303:1532–1535. <https://doi.org/10.1126/science.1092385>
- Caforio, A.L., S. Pankuweit, E. Arbustini, C. Basso, J. Gimeno-Blanes, S.B. Felix, M. Fu, T. Heliö, S. Heymans, R. Jahns, et al. European Society of Cardiology Working Group on Myocardial and Pericardial Diseases. 2013. Current state of knowledge on aetiology, diagnosis, management, and therapy of myocarditis: a position statement of the European Society of

- Cardiology Working Group on Myocardial and Pericardial Diseases. *Eur. Heart J.* 34:2636–2648: 2648a–2648d. <https://doi.org/10.1093/eurheartj/ehz210>
- Cooper, L.T. Jr., A. Keren, K. Sliwa, A. Matsumori, and G.A. Mensah. 2014. The global burden of myocarditis: part 1: a systematic literature review for the Global Burden of Diseases, Injuries, and Risk Factors 2010 study. *Glob. Heart.* 9:121–129. <https://doi.org/10.1016/j.gheart.2014.01.007>
- Ding, Z.M., J.E. Babensee, S.I. Simon, H. Lu, J.L. Perrard, D.C. Bullard, X.Y. Dai, S.K. Bromley, M.L. Dustin, M.L. Entman, et al. 1999. Relative contribution of LFA-1 and Mac-1 to neutrophil adhesion and migration. *J. Immunol.* 163:5029–5038.
- Epelman, S., P.P. Liu, and D.L. Mann. 2015. Role of innate and adaptive immune mechanisms in cardiac injury and repair. *Nat. Rev. Immunol.* 15:117–129. <https://doi.org/10.1038/nri3800>
- Grabmaier, U., H.D. Theiss, A. Keithahn, J. Kreiner, C. Brenner, B. Huber, C. von der Helm, L. Gross, K. Klingel, W.M. Franz, and S. Brunner. 2014. The role of 1.5 tesla MRI and anesthetic regimen concerning cardiac analysis in mice with cardiomyopathy. *PLoS One.* 9:e94615. <https://doi.org/10.1371/journal.pone.0094615>
- Herter, J.M., and T.N. Mayadas. 2014. Midkine, a middle manager of $\beta 2$ integrins. *Blood.* 123:1777–1779. <https://doi.org/10.1182/blood-2014-02-553073>
- Heymans, S., U. Eriksson, J. Lehtonen, and L.T. Cooper Jr. 2016. The Quest for New Approaches in Myocarditis and Inflammatory Cardiomyopathy. *J. Am. Coll. Cardiol.* 68:2348–2364. <https://doi.org/10.1016/j.jacc.2016.09.937>
- Horckmans, M., L. Ring, J. Duchene, D. Santovito, M.J. Schloss, M. Drechsler, C. Weber, O. Soehnlein, and S. Steffens. 2017. Neutrophils orchestrate post-myocardial infarction healing by polarizing macrophages towards a reparative phenotype. *Eur. Heart J.* 38:187–197.
- Jorch, S.K., and P. Kubes. 2017. An emerging role for neutrophil extracellular traps in noninfectious disease. *Nat. Med.* 23:279–287. <https://doi.org/10.1038/nm.4294>
- Kenny, E.F., A. Herzig, R. Krüger, A. Muth, S. Mondal, P.R. Thompson, V. Brinkmann, H.V. Bernuth, and A. Zychlinsky. 2017. Diverse stimuli engage different neutrophil extracellular trap pathways. *eLife.* 6:e24437. <https://doi.org/10.7554/eLife.24437>
- Kojima, S., T. Inui, H. Muramatsu, Y. Suzuki, K. Kadomatsu, M. Yoshizawa, S. Hirose, T. Kimura, S. Sakakibara, and T. Muramatsu. 1997. Dimerization of midkine by tissue transglutaminase and its functional implication. *J. Biol. Chem.* 272:9410–9416. <https://doi.org/10.1074/jbc.272.14.9410>
- Ley, K., C. Laudanna, M.I. Cybulsky, and S. Nourshargh. 2007. Getting to the site of inflammation: the leukocyte adhesion cascade updated. *Nat. Rev. Immunol.* 7:678–689. <https://doi.org/10.1038/nri2156>
- Lillis, A.P., L.B. Van Duyn, J.E. Murphy-Ullrich, and D.K. Strickland. 2008. LDL receptor-related protein 1: unique tissue-specific functions revealed by selective gene knockout studies. *Physiol. Rev.* 88:887–918. <https://doi.org/10.1152/physrev.00033.2007>
- Martinod, K., T. Witsch, L. Erpenbeck, A. Savchenko, H. Hayashi, D. Cherpokova, M. Gallant, M. Mauler, S.M. Cifuni, and D.D. Wagner. 2017. Peptidylarginine deiminase 4 promotes age-related organ fibrosis. *J. Exp. Med.* 214:439–458. <https://doi.org/10.1084/jem.20160530>
- Maruyama, K., H. Muramatsu, N. Ishiguro, and T. Muramatsu. 2004. Midkine, a heparin-binding growth factor, is fundamentally involved in the pathogenesis of rheumatoid arthritis. *Arthritis Rheum.* 50:1420–1429. <https://doi.org/10.1002/art.20175>
- McDonald, B., R.P. Davis, S.J. Kim, M. Tse, C.T. Esmon, E. Kolaczowska, and C.N. Jenne. 2017. Platelets and neutrophil extracellular traps collaborate to promote intravascular coagulation during sepsis in mice. *Blood.* 129:1357–1367. <https://doi.org/10.1182/blood-2016-09-741298>
- Muramatsu, T. 2014. Structure and function of midkine as the basis of its pharmacological effects. *Br. J. Pharmacol.* 171:814–826. <https://doi.org/10.1111/bph.12353>
- Muramatsu, T., and K. Kadomatsu. 2014. Midkine: an emerging target of drug development for treatment of multiple diseases. *Br. J. Pharmacol.* 171:811–813. <https://doi.org/10.1111/bph.12571>
- Nakazawa, D., S.V. Kumar, J. Marschner, J. Desai, A. Holderied, L. Rath, F. Kraft, Y. Lei, Y. Fukasawa, G.W. Moeckel, et al. 2017. Histones and Neutrophil Extracellular Traps Enhance Tubular Necrosis and Remote Organ Injury in Ischemic AKI. *J. Am. Soc. Nephrol.* 28:1753–1768. <https://doi.org/10.1681/ASN.2016080925>
- Netsu, S., T. Shishido, T. Kitahara, Y. Honda, A. Funayama, T. Narumi, S. Kadowaki, H. Takahashi, T. Miyamoto, T. Arimoto, et al. 2014. Midkine exacerbates pressure overload-induced cardiac remodeling. *Biochem. Biophys. Res. Commun.* 443:205–210. <https://doi.org/10.1016/j.bbrc.2013.11.083>
- Novotny, W.F., T. Maffi, R.L. Mehta, and P.G. Milner. 1993. Identification of novel heparin-releasable proteins, as well as the cytokines midkine and pleiotrophin, in human postheparin plasma. *Arterioscler. Thromb.* 13:1798–1805. <https://doi.org/10.1161/01.ATV.13.12.1798>
- Pick, R., D. Begandt, T.J. Stocker, M. Salvermoser, S. Thome, R.T. Böttcher, E. Montanez, U. Harrison, I. Forné, A.G. Khandoga, et al. 2017. Coronin 1A, a novel player in integrin biology, controls neutrophil trafficking in innate immunity. *Blood.* 130:847–858. <https://doi.org/10.1182/blood-2016-11-749622>
- Prasad, J.M., M. Migliorini, R. Galisteo, and D.K. Strickland. 2015. Generation of a Potent Low Density Lipoprotein Receptor-related Protein 1 (LRP1) Antagonist by Engineering a Stable Form of the Receptor-associated Protein (RAP) D3 Domain. *J. Biol. Chem.* 290:17262–17268. <https://doi.org/10.1074/jbc.M115.660084>
- Ranganathan, S., C. Cao, J. Catania, M. Migliorini, L. Zhang, and D.K. Strickland. 2011. Molecular basis for the interaction of low density lipoprotein receptor-related protein 1 (LRP1) with integrin α M β 2: identification of binding sites within α M β 2 for LRP1. *J. Biol. Chem.* 286:30535–30541. <https://doi.org/10.1074/jbc.M111.265413>
- Redecke, V., R. Wu, J. Zhou, D. Finkelstein, V. Chaturvedi, A.A. High, and H. Häcker. 2013. Hematopoietic progenitor cell lines with myeloid and lymphoid potential. *Nat. Methods.* 10:795–803. <https://doi.org/10.1038/nmeth.2510>
- Rose, N.R. 2014. Learning from myocarditis: mimicry, chaos and black holes. *F1000Prime Rep.* 6:25. <https://doi.org/10.12703/P6-25>
- Smith, S.C., and P.M. Allen. 1991. Myosin-induced acute myocarditis is a T cell-mediated disease. *J. Immunol.* 147:2141–2147.
- Sørensen, O.E., and N. Borregaard. 2016. Neutrophil extracellular traps - the dark side of neutrophils. *J. Clin. Invest.* 126:1612–1620. <https://doi.org/10.1172/JCI84538>
- Spijkers, P.P., P. da Costa Martins, E. Westein, C.G. Gahmberg, J.J. Zwaginga, and P.J. Lenting. 2005. LDL-receptor-related protein regulates $\beta 2$ -integrin-mediated leukocyte adhesion. *Blood.* 105:170–177. <https://doi.org/10.1182/blood-2004-02-0498>
- Stark, K., A. Eckart, S. Haidari, A. Tirniceru, M. Lorenz, M.L. von Brühl, F. Gärtner, A.G. Khandoga, K.R. Legate, R. Pless, et al. 2013. Capillary and arteriolar pericytes attract innate leukocytes exiting through venules and 'instruct' them with pattern-recognition and motility programs. *Nat. Immunol.* 14:41–51. <https://doi.org/10.1038/ni.2477>
- Sumida, A., M. Horiba, H. Ishiguro, H. Takenaka, N. Ueda, H. Ooboshi, T. Ophof, K. Kadomatsu, and I. Kodama. 2010. Midkine gene transfer after myocardial infarction in rats prevents remodeling and ameliorates cardiac dysfunction. *Cardiovasc. Res.* 86:113–121. <https://doi.org/10.1093/cvr/cvp386>
- Takenaka, H., M. Horiba, H. Ishiguro, A. Sumida, M. Hojo, A. Usui, T. Akita, S. Sakuma, Y. Ueda, I. Kodama, and K. Kadomatsu. 2009. Midkine prevents ventricular remodeling and improves long-term survival after myocardial infarction. *Am. J. Physiol. Heart Circ. Physiol.* 296:H462–H469. <https://doi.org/10.1152/ajpheart.00733.2008>
- Tillack, K., P. Breiden, R. Martin, and M. Sospedra. 2012. T lymphocyte priming by neutrophil extracellular traps links innate and adaptive immune responses. *J. Immunol.* 188:3150–3159. <https://doi.org/10.1049/jimmunol.1103414>
- Toussaint, M., D.J. Jackson, D. Swieboda, A. Guedán, T.D. Tsourouktsoglou, Y.M. Ching, C. Radermecker, H. Makrinioti, J. Aniscenko, N.W. Bartlett, et al. 2017. Host DNA released by NETosis promotes rhinovirus-induced type-2 allergic asthma exacerbation. *Nat. Med.* 23:681–691. <https://doi.org/10.1038/nm.4332>
- Valapert, A., R.R. Marty, G. Kania, D. Germano, N. Mauermann, S. Dirnhofer, B. Leimenstoll, P. Blyszczuk, C. Dong, C. Mueller, et al. 2008. CD11b⁺ monocytes abrogate Th17 CD4⁺ T cell-mediated experimental autoimmune myocarditis. *J. Immunol.* 180:2686–2695. <https://doi.org/10.1049/jimmunol.180.4.2686>
- Wang, G.G., K.R. Calvo, M.P. Pasillas, D.B. Sykes, H. Häcker, and M.P. Kamps. 2006. Quantitative production of macrophages or neutrophils ex vivo using conditional Hoxb8. *Nat. Methods.* 3:287–293. <https://doi.org/10.1038/nmeth865>
- Wang, J., H. Takeuchi, Y. Sonobe, S. Jin, T. Mizuno, S. Miyakawa, M. Fujiwara, Y. Nakamura, T. Kato, H. Muramatsu, et al. 2008. Inhibition of midkine alleviates experimental autoimmune encephalomyelitis through the expansion of regulatory T cell population. *Proc. Natl. Acad. Sci. USA.* 105:3915–3920. <https://doi.org/10.1073/pnas.0709592105>

- Warnatsch, A., M. Ioannou, Q. Wang, and V. Papayannopoulos. 2015. Inflammation. Neutrophil extracellular traps license macrophages for cytokine production in atherosclerosis. *Science*. 349:316–320. <https://doi.org/10.1126/science.aaa8064>
- Weckbach, L.T., L. Groesser, J. Borgolte, J.I. Pagel, F. Pogoda, J. Schymeinsky, J. Müller-Höcker, M. Shakibaei, T. Muramatsu, E. Deindl, and B. Walzog. 2012. Midkine acts as proangiogenic cytokine in hypoxia-induced angiogenesis. *Am. J. Physiol. Heart Circ. Physiol.* 303:H429–H438. <https://doi.org/10.1152/ajpheart.00934.2011>
- Weckbach, L.T., A. Gola, M. Winkelmann, S.M. Jakob, L. Groesser, J. Borgolte, F. Pogoda, R. Pick, M. Pruenster, J. Müller-Höcker, et al. 2014. The cytokine midkine supports neutrophil trafficking during acute inflammation by promoting adhesion via $\beta 2$ integrins (CD11/CD18). *Blood*. 123:1887–1896. <https://doi.org/10.1182/blood-2013-06-510875>
- Willeke, T., S. Behrens, K. Scharffetter-Kochanek, P. Gaehtgens, and B. Walzog. 2000. Beta2 integrin (CD11/CD18)-mediated signaling involves tyrosine phosphorylation of c-Cbl in human neutrophils. *J. Leukoc. Biol.* 68:284–292.
- Zehrer, A., R. Pick, M. Salvermoser, A. Boda, M. Miller, K. Stark, L.T. Weckbach, B. Walzog, and D. Begandt. 2018. A Fundamental Role of Myh9 for Neutrophil Migration in Innate Immunity. *J. Immunol.* 201:1748–1764. <https://doi.org/10.4049/jimmunol.1701400>
- Zhang, R., Y. Pan, V. Fanelli, S. Wu, A.A. Luo, D. Islam, B. Han, P. Mao, M. Ghazarian, W. Zeng, et al. 2015. Mechanical Stress and the Induction of Lung Fibrosis via the Midkine Signaling Pathway. *Am. J. Respir. Crit. Care Med.* 192:315–323. <https://doi.org/10.1164/rccm.201412-2326OC>